Title
Factors that can influence the onset time of rapid intensification of tropical cyclones

Author
Bu, Yizhe

Publication Date
2012

Peer reviewed|Thesis/dissertation

UNIVERSITY OF CALIFORNIA

Los Angeles

Factors That Can Influence the Onset Time of Rapid Intensification of Tropical Cyclones

A thesis submitted in partial satisfaction

of the requirements for the degree

Master of Science in Atmospheric and Oceanic Sciences

by

Yizhe Bu

2012

ABSTRACT OF THE THESIS

Factors That Can Influence the Onset Time of Rapid Intensification of Tropical Cyclones

by

Yizhe Bu

Master of Science in Atmospheric and Oceanic Sciences

University of California, Los Angeles, 2012

Professor Robert Fovell, Chair

An axisymmetric version of the Bryan Cloud Model (CM1) is used to determine how quickly a coherent and relatively stable tropical cyclone (TC) circulation can form from an initial vortex of nominal intensity. Some of the factors that may influence the onset time of the rapid intensification are examined, including the height of the tropopause, the microphysical parameterizations, the midlevel dryness and the total surface heat flux from the sea surface. Our analyses of these simulations suggest that there are two conditions that need to be satisfied before RI can occur: the vertical structure of the middle troposphere has to become moist adiabatic in the inner core and peripheral convection has to become suppressed or merged with convection in the inner region.

The thesis of Yizhe Bu is approved.

Kuo-Nan Liou

Alex Hall

Robert Fovell, Committee Chair

University of California, Los Angeles

2012

Table of Contents

List of Figures

CHAPTER 1

Introduction

There are several competing theories concerned with the generation and intensification of tropical cyclones (TCs), such as CISK (*Ooyama*, 1964; *Charney and Eliassen*, 1964) and WISHE (*Emanuel*, 1986, 1994; *Holton*, 2004). According to CISK, or Convective Instability of the Second Kind, TC development starts with a low surface pressure perturbation over the sea. Surface air spirals into the surface low, resulting in mass convergence and forcing ascent. Water vapor condenses out from the rising air, releasing the latent heat into the air, which generates a large-scale (or mesoscale) cyclonic disturbance, which then drives additional the low-level moisture convergence through boundary layer pumping. The sea surface pressure under this warm region decreases further as the warm air is less dense than the surrounding cool air, amplifying the horizontal pressure gradient. This causes more surface convergence and more warm moist surface air to rise up, releasing even more latent heat. Once this cycle established, it is self-sustaining, at least until the TC encounters external factors that can serve to cause weakening, such as the strong wind shear, dry land and/or cold sea surface temperatures (SSTs).

However, the intensification rate of a TC has been found to have a strong positive dependence on heat and moisture transfer coefficients, factors that control the flux of energy between the ocean and atmosphere (*Craig and Gray*, 1996). CISK does not predict the observed dependence on heat and moisture transfer coefficients as its entire focus is on the instability of the atmosphere. The ability of the storm to induce moist convection is measured by the convective available potential energy (CAPE) of its

surrounding environment. The initial CAPE is rapidly consumed. The energy coming from the cumulus convection may not be large enough at any given moment.

In 1986, Emanuel proposed WISHE as an alternative to CISK (*Emanuel*, 1986). The term WISHE stands for Wind-Induced Surface Heat Exchange. In WISHE, the potential energy for hurricanes arises from the thermodynamic disequilibrium between the atmosphere and the underlying ocean. It requires sufficient latent heat to balance frictional dissipation. The surface fluxes, including heat and moisture are wind speed dependent and, therefore, determined by the vortex-scale flow. Therefore, the positive feedback between the near-surface θ_e and the near-surface wind speed is important for vortex intensification. The intensification mechanism of WISHE does predict the observed increases in intensification rate with heat and moisture transfer coefficients (*Craig and Gray*, 1996).

Beyond those two mechanisms, there are other factors that can influence TC organization rates and their final intensities, such as height of the tropopause, cloud microphysical processes and assumptions, the peripheral convection, middle-level water content, and size of the initial vortex. We will look at each of these in turn.*Emanuel* (1986) points out that the tropopause height can influence the steady-state intensity of the TC via changing the outflow temperature. The relationship between them is:

$$ln\pi_{cs} \approx \frac{-(\frac{T_B-\overline{T}_{out}}{T_B})\frac{Lq_a^*}{C_pT_s}(RH_c - RH_a)_s + \frac{1}{4}\frac{f^2r_0^2}{C_pT_B}}{1-(\frac{T_B-\overline{T}_{out}}{T_B})(1+\frac{Lq_a^*RH_{cs}}{RT_s})} \tag{1.1}$$

where π_s is the central surface pressure, T_B is the absolute temperature at the top of the boundary layer, T_{out} is an average outflow temperature, RH_c is the relative humidity in the core, and RH_a is the ambient relative humidity. Emanuel envisioned the TC as a Carnot heat engine, the efficiency of which is determined by the temperature difference between warm and cold thermal reservoirs. Here, the warm thermal reservoir is the ocean and the outflow temperature is effectively that of the tropopause. The $\frac{T_B-\overline{T}_{out}}{T_B}$

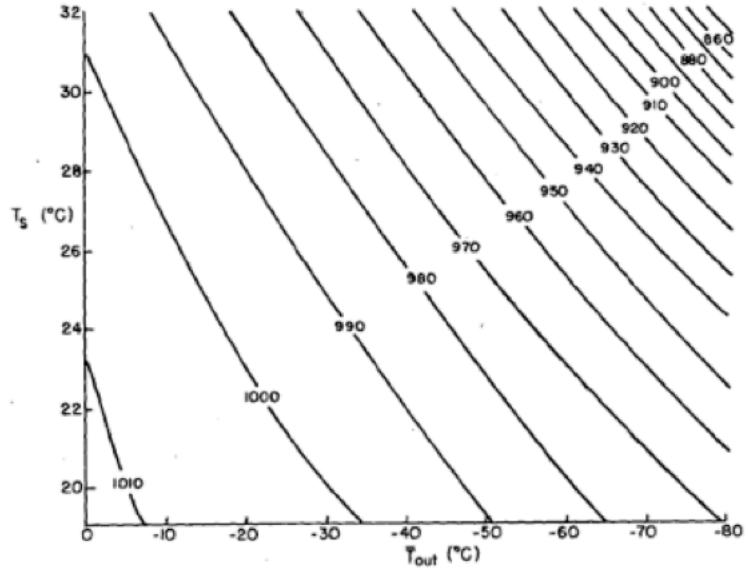

Figure 1.1: Minimum attainable central surface pressure (mb) computed from the equation on the left as a function of surface air temperature (Ts) and weighted mean outflow temperature assuming an ambient surface pressure of 1015 mb, ambient surface relative humidity of 80%. From *Emanuel* (1986)

term represents the thermodynamic efficiency.

Thus, the outflow from the cyclone should be cold enough to account for a reasonable thermodynamic efficiency. Figure 1.1, taken from *Emanuel* (1986), demonstrates that TC intensity increases with decreasing outflow temperature when the SST is fixed. In a typical (tropical) environment, the tropopause represents a local minimum temperature that can be expected to be lower as tropopause elevation rises. Therefore, he argues that TC intensity is positively associated with tropopause height.

Cloud microphysics refers to the processes that control how condensed water vapor evolves and moves vertically through the atmosphere. Some cloud microphysical parameterizations are quite simple, while others are enormously complex and contain a large number of relatively poorly constrained or understood parameters and factors. A warm rain scheme, such as that proposed by *Kessler* (1969), results when frozen water

is completely neglected. Among the ice species that might be considered include free-floating cloud ice, low-density aggregates like snow, and denser hydrometeors such as groupel and hail. Mixed phase schemes permit frozen and liquid condensate to coexist and interact.

Changing cloud microphysical assumptions can alter TC structure, including radial winds and azimuthal asymmetries (*Fovell et al.*, 2009, 2010) and vertical heating rates (*Zhu and Zhang*, 2006), impacting intensity (e.g., *Lord et al.* (1984); *Wang* (2002); *Zhu and Zhang* (2006)) as well as track (*Fovell et al.*, 2009, 2010). In particular, *Wang* (2002) showed markedly different intensities and intensification rates resulted when frozen hydrometers were included or melting and evaporation were neglected (see his Fig. 2). In some studies, the warm-rain microphysics scheme tends produce TCs that intensity quickly and/or attain the strongest intensities (e.g., *Hausman et al.* (2006); *Li and Pu.* (2008); *Stern and Nolan* (2012), but in others results in relatively weaker storms (e.g., *Wang* (2002); *Zhu and Zhang* (2006); *Fovell et al.* (2009)). This suggests that microphysical processes are important, and an integral part of uncertainty.

Near saturation of the air column at the vortex core appears to be necessary for intensification (*Emanuel*, 1995; *Emanuel et al.*, 2004) because midlevel dryness presents a significant barrier to the development of TCs (*Emanuel*, 1994). *Emanuel et al.* (1994) argue that TC amplification requires the middle troposphere to become nearly saturated so that the downdrafts would be too weak to offset the moistening of the boundary layer via surface fluxes. Besides, *Bister* (2001) shows that the inner region must be very humid before the rapid intensification can start. Figure 1.2 shows the time histories of relative humidity for three experiments Bister performed, called TR (Tropics), ST (subtropics) and 20deg (whose Coriolis parameter is the mean value in experiments TR and ST). In experiment TR, ST and 20deg, their RI of the vortex starts at hour 70, 150 and 100, respectively. Relating to the relative humidity evolution, their rapid intensification begins when the averaged relative humidity reaches a value of 90%. Here,

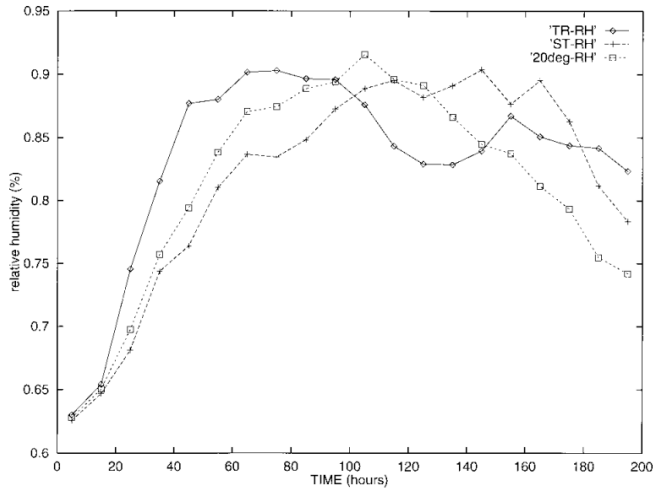

Figure 1.2: Relative humidity within the inner 100 km in experiments TR, ST, and 20°. Averages are taken over radius from the height of 0.625 to 5.625 km. From Bister (2001)

rapid intensification (RI) is satisfied when a TCs minimum surface pressure decreases by at least 42 mb in a 24 hour period (*Holliday and Thompson*, 1979).

The size of the initial vortex can matter as well. When vortex is a large, its initial convection will spread over a very broad area. As a result, the central or inner core region cannot become moist enough to prevent cool downdrafts from keeping θ_e low in the boundary layer (*Emanuel*, 1986). The inner core defined by *Weatherford and Gray* (1988) extends from the TC center to 1° latitude radius, contrasted with the outer core zone which is defined as the region between radii of 1° and 2.5°.

Thus, it would appear that decreasing the amount of outer core convection would result in an earlier onset of RI of the vortex into a TC. *Bister* (1997) showed that the consequence of outer convection was to not only increase the tangential wind in the outer region but also decrease it through most of the inner region. These changes are unfavorable for inner convection. *Bister* (2001) conducts an experiment, in which the sea surface fluxes were set to zero outside the radius of 184 km. This prevents strong outer convection from occurring outside the radius of 150 km. This vortex intensifies 14 h earlier than when the sea surface heat fluxes are allowed at all radii.

Wang (2009) pointed out that the outer spiral rainbands can hurt the eyewall formation from both dynamic and thermodynamic aspects. Dynamically, the mass convergence into spiral rainbands may reduce the mass convergence into the eyewall, which will decrease the eyewall updrafts and convection. Additionally, the outer rainbands can block the boundary layer inflow, injuring the eyewall circulation. Thermodynamically, strong downdrafts associated with the strong convection in outer spiral rainbands can bring low equivalent potential temperature (θ_e) air from the middle troposphere down to the inflow boundary layer. As a result, the eyewall buoyancy and thus the TC intensity will be reduced (*Barnes et al.*, 1983; *Powell*, 1990a,b). The other thermodynamic effect is that the diabatic heating in outer spiral rainbands may cause the pressure to fall in the lower troposphere and reduce the horizontal pressure gradient across the radius of maximum winds (RMW), which will weaken the tangential wind there.

Whereas the above arguments suggest that the outer rainbands weaken the storm intensity, there are reasons to suspect that rainband convection can help support or even intensify a TC. Following the papers of *Hoskins et al.* (1985) and *Davis and Emanuel* (1991), numerous studies have utilized the potential vorticity (PV) framework for the study of TCs (e.g., *Molinari et al.* (1998); *Davis and Bosart* (2001, 2002)). Mathematically, Ertels form of PV is given by the equation:

$$PV = \frac{1}{\rho}\zeta^a \cdot \nabla\theta \tag{1.2}$$

where ζ^a is the absolute vorticity. Cyclonic PV is generated by latent heat release in outer spiral rainbands. The transfer of this cyclonic PV to the TC core region could be a considerable PV source to the TC core. The PV moving along the spiral band may affect the cyclone core in two ways. One is that the downward PV flux to the surface may directly supply vorticity to the low-level flow. Additionally, the substantial concentration of vorticity may play an important role in secondary eyewall generation.

As a result, spiral rainbands might act to increase TC intensity (*May and Holland*, 1999; *Hill and Lackmann*, 2009).

Outer core convection can itself be modulated via the relative humidity (RH) of the environment beyond the inner core. Recently, *Braun et al.* (2012) investigated the influence of dry layers on TC development, motivated by a phenomenon called the Saharan Air Layer (SAL). They inserted midlevel dry tongue mimicking the low RH aspect of the SAL at various distances and orientations relative to the initial TC vortex. Figure 1.3 summarizes some of their results, which are divided into 2 sets. The first set of simulations begins with dry air located north of the vortex at various distances from the center, including DRY0 (0 km from TC center), DRY90 (90 km), DRY144 (144 km) and DRY270 (270 km), while the second set begins with dry air completely surrounding the vortex at various radii, including DRYALL0 (0 km from TC center), DRYALL75 (75 km) and DRYALL150 (150km).

Relative to a control run (CNTL) having no dry tongue, nearly every experiment in the *Braun et al.* (2012) study shows that the presence of dry midlevel air delays that ability of the incipient TC to organize. Furthermore, the closer the dry tongue is to the storm, the more severe and long-lasting its impact. Besides, at the same distance, the presence of a moist envelope around the vortex center eliminates the deleterious impact on storm intensity, compared with the simulations in which the dry air is located north of the TC center. This is explained as a consequence of low RH air intrusions into the inner core. *Braun et al.* (2012) point out that the intensification rate impact involves an outwardly spiraling asymmetric rainband that increasingly delays storm development. As long as the dry air permits a symmetric zone of convection in the eyewall, it does not necessarily inhibit intensification, such as DRYALL75, which produces the most downdraft cooling and yet intensifies at a rate similar to CNTL.

Yet, owing to the apparently deleterious impact of rainband convection, and the fact that this might be restrained by the presence of low environmental RH in the

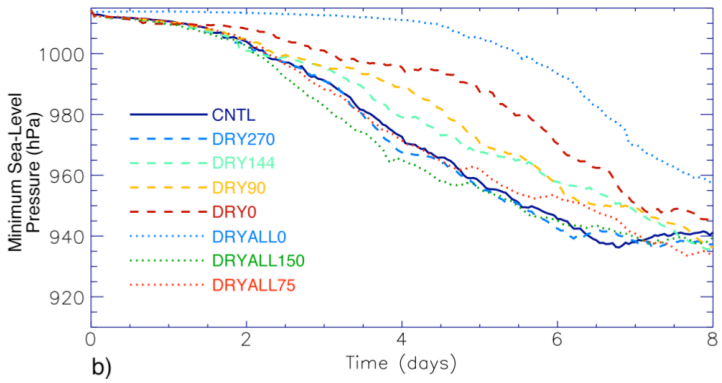

Figure 1.3: Time histories of minimum SLP for all simulations. The solid line is the control run, the dashed lines are the runs with dry air north of specified latitude, and the dotted lines are for runs with dry air throughout the domain except for a moist envelope within the vortex.

right place, we find it curious that there was no experiment in which the dry tongue dramatically aids TC development. However, if we have a closer look at the Figure, the DRYALL150 run actually makes the intensification a little bit earlier though the tendency is not significant.

In this report, we use an axisymmetric model starting with a fairly robust vortex and a very favorable environmental condition to examine the organization of TCs. By design, an axisymmetric model possesses neither azimuthal asymmetries (which are suspected of weakening storms; e.g., *Nolan and Grasso* (2003); *Nolan et al.* (2007)) nor supports outward-propagating vortex Rossby waves that appear to play a role at least in the inner rainbands, so those potentially complicating factors are controlled via their absence. In particular, we will be concerned with that we will call the tipping point, the time at which TC development finally starts to proceed inexorably, if not especially quickly. In moist experiments, the tipping point is followed immediately by a period of RI, such that it is also the RI onset time.

Figure 1.4 presents time histories of minimum sea-level pressure (SLP) for several simulations, made using the axisymmetric model to be described in the next chapter. The control run, which using the Kessler cloud microphysics scheme, takes two and

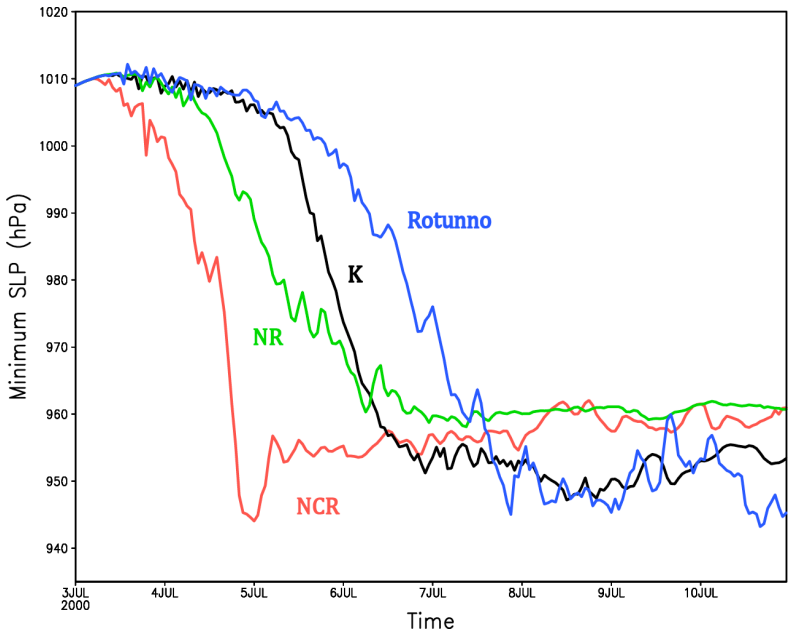

Figure 1.4: Time histories of minimum SLP in several experiments using the Kessler (black), NCR (red), NR (green) and Rotunno (blue) microphysics schemes.

a half days before the commencement of RI. The figure also shows histories for the NCR, NR and Rotunno (*Rotunno and Emanuel*, 1987) schemes. NR and NCR are all based on Kessler; for NR, rain is prevented from forming, and for NCR, all condensate is immediately removed from the domain (this was termed the no-cloud cloud model in *Fovell* (2004)). Rotunno's scheme is also Kessler-like, but folds cloud droplets and rain water into a single prognostic variable.

It is seen that the model TCs differ markedly in two respects: how long it takes for the storm to organize, and how quickly organization can take place. While all four TCs eventually reach the same minimum central pressures of about 950 mb after about 4 days, the Rotunno storm is definitely the slowest developer of the group, taking 72 h before finally reaching the tipping point. In contrast, the NCR run takes less than 12 h to achieve RI. In this case, neither final intensities nor the intensification rate is the decisive factor. The two TCs differed with respect to how quickly they could develop into mature TC vortices.

This report focuses on the factors that may control the length of the TC gestation period. In Chapter 3, we examine the aforementioned factors of tropopause height, microphysical assumptions and the surface heat flux. From these experiments, we conclude that there are two necessary conditions that need to be satisfied before RI can occur: one is the environment needs to achieve an approximately moist adiabatic state in the inner core region, and the other is the strong peripheral (outer core) convection needs to be either suppressed or merged with the inner convection. These two conditions and their influence on the tipping point is the subject of Chapter 4.

CHAPTER 2

Model and Experimental Design

The numerical experiments are carried out using an axisymmetric version of the Bryan Cloud Model (CM1, revision 14) (*Bryan and Fritsch*, 2002; *Bryan and Rotunno*, 2009). All of the experiments are initialized with the approximately moist-neutral hurricane sounding (*Rotunno and Emanuel*, 1987) except for one experiment in which a moist adiabatic profile was used. The SST is 26.15°C and held fixed. All experiments employ a horizontal resolution of 1 km and a vertical grid spacing of 0.25 km. The domain is 800 km wide and 25 km deep. The lateral boundaries and the top boundary of the domain are all rigid.

To initiate motion in the domain, we adopt the Rotunno-Emanuel initialization (*Rotunno and Emanuel*, 1987), inserting a wide and gentle vortex with a 15 m/s maximum tangential velocity at a radius of 82.5 km (Figure 2.1) into the initial field. Each simulation is integrated for 7 days, commencing at the arbitrary date of 3 July 2000. As mentioned in Chapter 1, the Kessler cloud microphysics scheme is adopted with no changes for the control run. Most of the simulations show in this report use various versions of this very simple warm rain scheme, which will be further described as needed.

One of our experiments in Chapter 3 will focus on the influence of the tropopause height. This variation is accomplished through altering the vertical profile of potential temperature without changing either the tropospheric or stratospheric lapse rates (Figure 2.2). We specifically consider tropopause heights of 11 km, 14 km, 17 km and 19

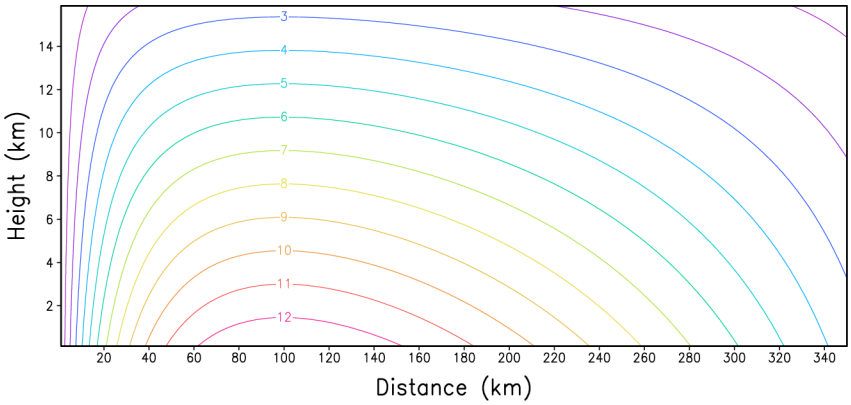

Figure 2.1: Tangential wind field at the initial time

km, with the 14 km level representing the control case. The transition layer between the two layers with different lapse rates is the tropopause.

In Chapter 4, we will compare simulations made with the control moist-neutral sounding with one that is initially moist adiabatic. The vertical profiles of θ_e for these two situations are shown in Figure 2.3.

In our analysis, we will compute budgets of absolute angular momentum (AAM), for which we adopt formula from *Holland* (1983) given by

$$M_a = M_r + M_e = rv + r(\Omega r sin\Phi_0) = rv + r^2 f_0/2 \tag{2.1}$$

In this equation, M_r is the relative angular momentum, M_e the earth angular momentum, v is the azimuthal wind speed and the other terms have their usual meanings.

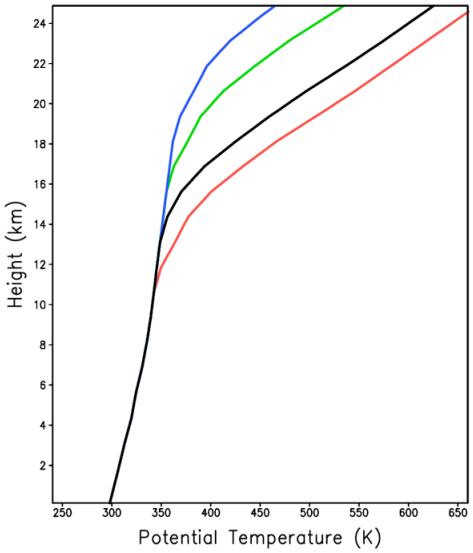

Figure 2.2: Initial vertical profiles of potential temperature (θ) for experiments placing the tropopause at 11 km (red), 14 km (black), 17 km (green) and 19 km (blue). The control run employs the 14 km tropopause height.

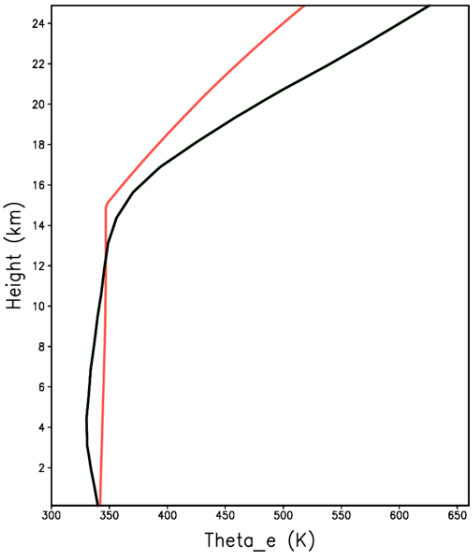

Figure 2.3: Initial vertical θ_e profile of moist adiabatic sounding (red) and approximately moist-neutral hurricane sounding (black)

CHAPTER 3

Results

3.1 Tropopause height variation

In addition to the control run, which employs the Kessler parameterization and possesses a tropopause placed at 14 km (tp14), simulations with tropopauses at 11 km (tp11), 17 km (tp17) and 19 km (tp19) are conducted by modifying the approximately moist-neutral hurricane sounding, as was shown in Figure 2.2. All of them share the same potential temperature profile in the troposphere and the same stratospheric lapse rate. Figure 3.1 shows their minimum SLP time histories, and Figure 3.2 presents fields of temperature, and outward radial and upward velocities averaged over the 144-192 h period during which each simulation is relatively steady, at least with respect to minimum SLP. Figure 3.3 presents time-averaged fields over the first 54 h of each run, which precedes the RI period.

As shown in Figure 3.2, the outflows are confined below 13 km and 15 km in the tp11 and tp14 runs, respectively, which are lower than they are in the tp17 and tp19 runs (both around 17 km). The maximum outflow level of cases tp17 and tp19 is near 14 km while the tp11 and tp14 runs have their maximum outflows at 10 km and 12.5 km, respectively. As a consequence of the tropospheric lapse rate, the outflow temperatures for tp17 and tp19 are colder than those of tp11 and tp14. As predicted by Emanuels (1986) theory, colder outflows are associated with deeper central pressures (Figure 3.1).

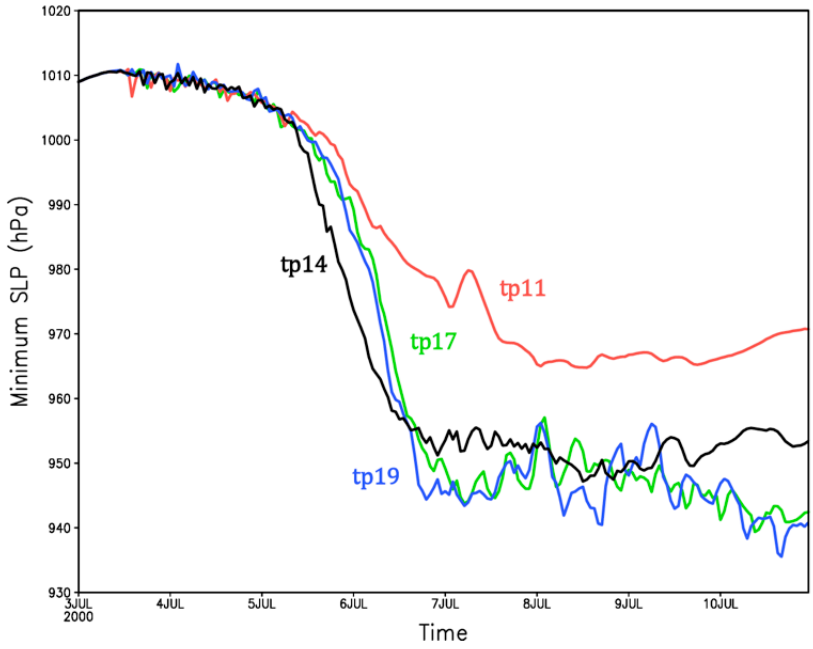

Figure 3.1: Time histories of minimum SLP for experiments having different tropopause heights of 11 km (red), 14 km (black), 17 km (green) and 19 km (blue).

In contrast, case tp11 clearly has the lowest and warmest tropopause and the weakest final intensity, with a minimum SLP about 20 mb higher than tp11 and 30 mb higher than runs tp17 and tp19. Furthermore, tp11 is the last of the four to reach its tipping point, and its subsequent deepening rate is not large enough enough to be deemed as RI. Curiously, the case with the intermediate tropopause height (tp14, the control run) reaches the tipping point first (about 6 h earlier), although consistent with the Emanuel theory it does wind up being less intense than the cases with the higher and colder tropopause. It is not presently clear why this is the case, although the discussion later in this chapter and in Chapter 4 is relevant to understanding this behavior.

Storms tp17 and tp19 are very similar throughout their integrations because their tropopauses reside above the equilibrium level for parcels ascending in the eyewall updraft, which means it is not a limiting factor for the storm circulation or the outflow temperature. Early on, case tp14 is also similar to that pair of storms because, as

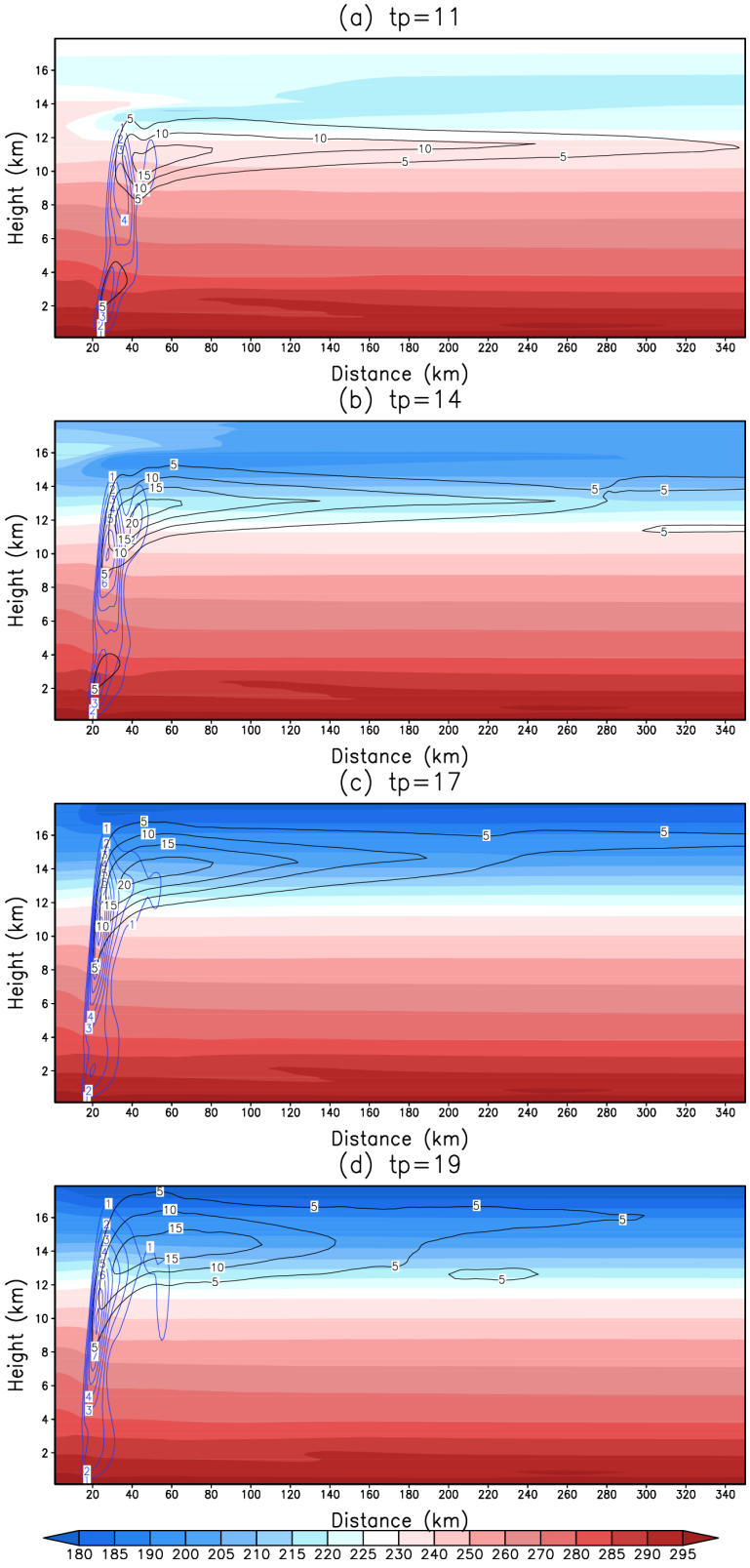

Figure 3.2: Temperature (color field), upward vertical velocity (blue contours) and outward radial velocity (black contours) averaged between 144-192 h for (a) tp11, (b) tp14 (control run), (c) tp17, and (d) tp19.

suggested by Figure 3.3, it takes time for the TC to develop vertically to the point where the control tropopause level becomes limiting. The tp11 case, however, is clearly already limited by its shallow troposphere. Its outflow temperature is at least 10°K higher than for the other cases.

In summary, the height of tropopause can influence the development of TC when it is near or below the parcel equilibrium level. Before the vertical development of the circulation becomes substantial, only a very low tropopause would impact storm organization. This applies to the tp11 case, which is the last of the four cases to reach its tipping point, and exhibits the slowest rate of development after that point. Storm tp14 takes longer to become mature limited by its tropospheric depth, while the remaining two cases exhibited little or no sensitivity to their tropopauses as those resided at heights beyond where their lofted parcels can reach.

3.2 Cloud microphysical parameterizations

In this section, we explore the model storms sensitivity to cloud microphysical parameterizations (MPs). Initially, we consider two liquid-only MPs, Kessler (K) and *Rotunno and Emanuel* (1987) simplified version of Kessler (Rotunno), and two schemes incorporating frozen condensate, the Goddard (*Tao and Simpson*, 1993) and Thompson schemes (*Thompson et al.*, 2004). Both Goddard and Thompson consider three forms of frozen water, being cloud ice, snow and graupel. However, as shown in Figure 3.4, the inclusion of ice does not by itself significantly influence either the tipping point or the intensification rate, although some influence on the final intensity can be noted, and the Rotunno storm develops relatively slowly. Therefore, to simplify the model and analysis, we consider only warm rain schemes from this point on, with the Kessler simulation still being the control run.

Two new warm rain variants are now introduced, based on the original Kessler

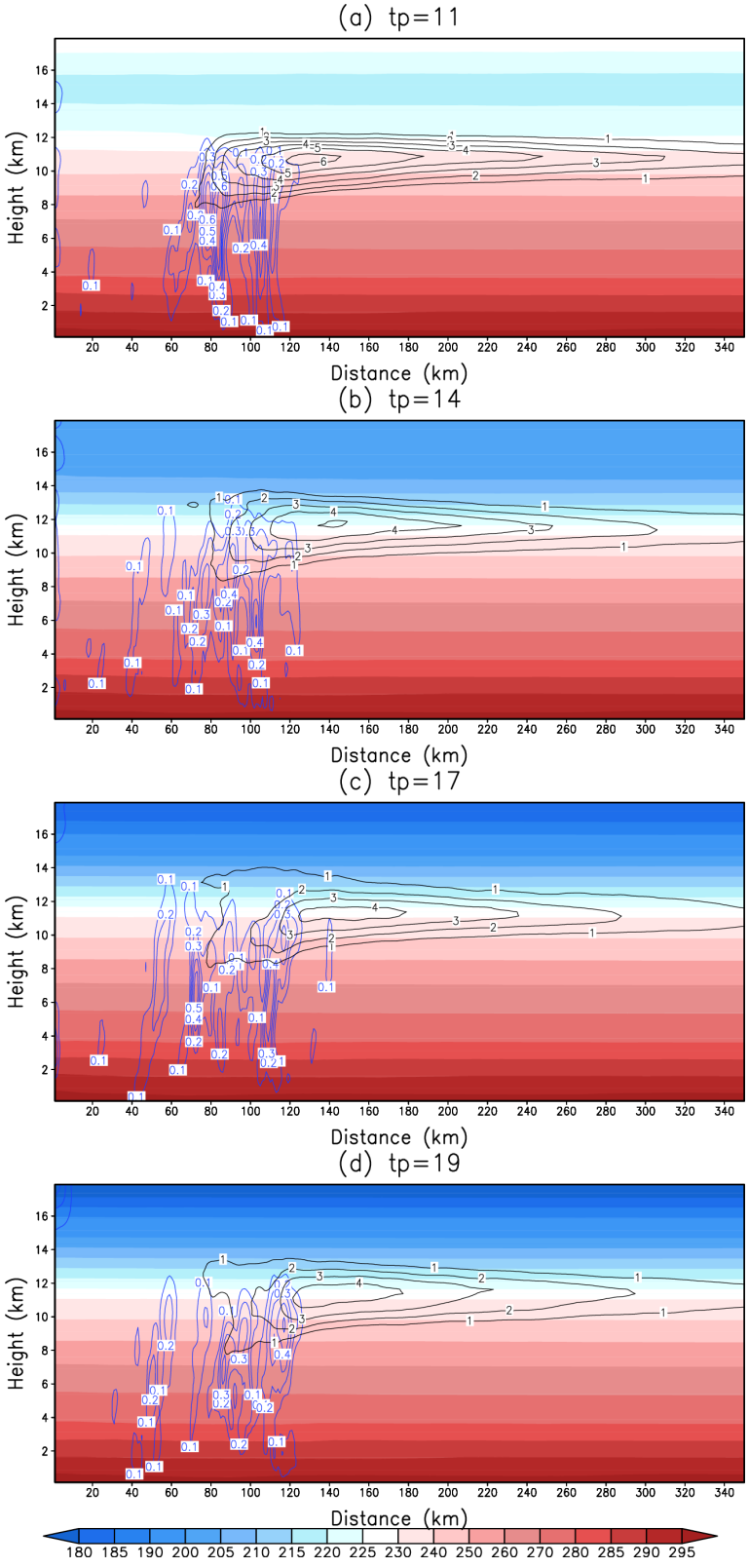

Figure 3.3: Same as Figure 9 but averaged from 1-54 h.

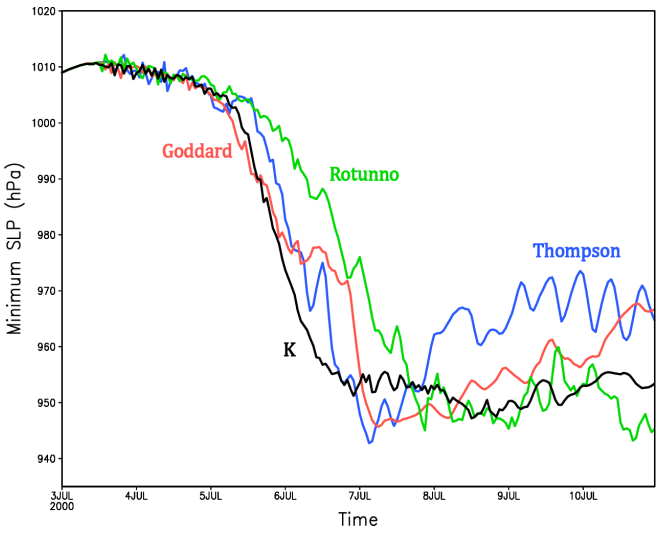

Figure 3.4: Time histories of minimum SLP in experiments Kessler (K), Goddard, Rotunno, and Thompson

scheme. For the NR (no rain) parameterization, rain is given an infinite fall speed, meaning that it is removed from the domain as quickly as it forms. For scheme NCR (no cloud and rain), all condensate is immediately removed from the domain as it is created (*Fovell*, 2004). As shown in Figure 3.5, the final intensities and RI rates of the three Kessler-like simulations are very close to each other but their tipping points are very different. The control run K requires more than 2 days to get organized while NCR and NR only take about 20 h and 36 h to commence RI, respectively.

Because NCR immediately removes all condensation everywhere in the domain, there is neither evaporation cooling nor water loading to drive downdrafts via negative buoyancy. As downdrafts can transport mid-level air with low equivalent potential temperature (θ_e) to the surface, one should expect that θ_e should be relatively larger at lower levels in the NCR run. Near-surface low θ_e air tends to reduce the convective instability, which should delay TC development. Therefore, it is reasonable that the NCR storm can organize quickly.

Figure 3.6 is a Hovmoller diagram of perturbation θ_e (with respect to the initial state) and vertical velocity at a height of 1 km for the first 48 h. As expected, the NCR

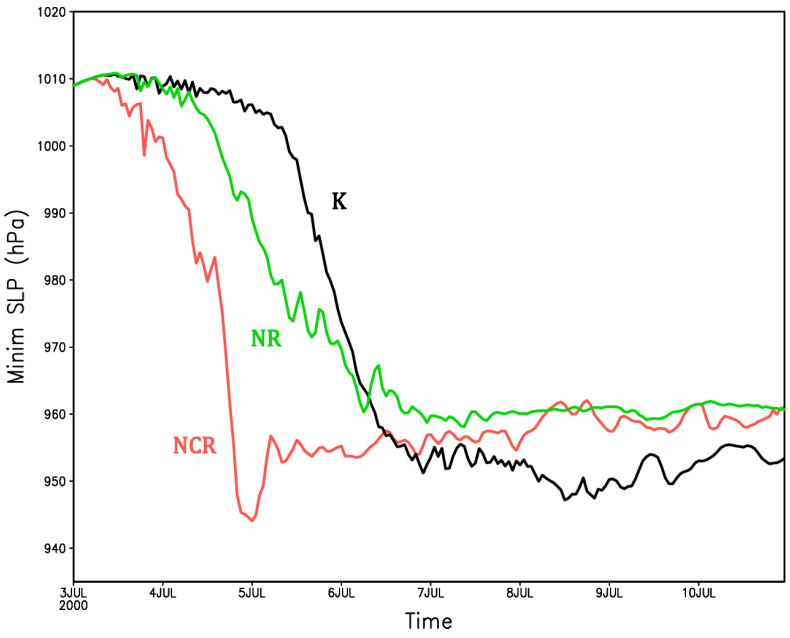

Figure 3.5: Time histories of minimum SLP in several experiments K, NCR and NR

case has little downdraft through the whole domain, except for very near the symmetry axis. After 10 h, an inward-propagating feature possessing locally very high θ_e can be seen. The control run has lower θ_e and stronger downdrafts but its perturbations are positive nearly everywhere in the inner core region, indicating the importance of fluxes of heat and moisture from the warm ocean surface. At least at this height level, it cannot warm up as quickly as the NCR case.

In the NR run, rainwater disappears from the domain as soon as it forms, but that does not mean that the total liquid water content (LWC) is low, as illustrated in Figure 3.7, which shows LWC and vertical velocity average from 10 h to 20 h for NR and control. In a Kessler-like MP, new rainwater is created from cloud droplets via the autoconversion process, but most of the rain mass source comes from accretion of cloud water as the raindrops fall relative to still air. This sink for cloud droplets is inactive in NR, permitting the LWC to become quite large, especially relative to the weak control run. The NR case still possesses hydrometeor drag and evaporation of

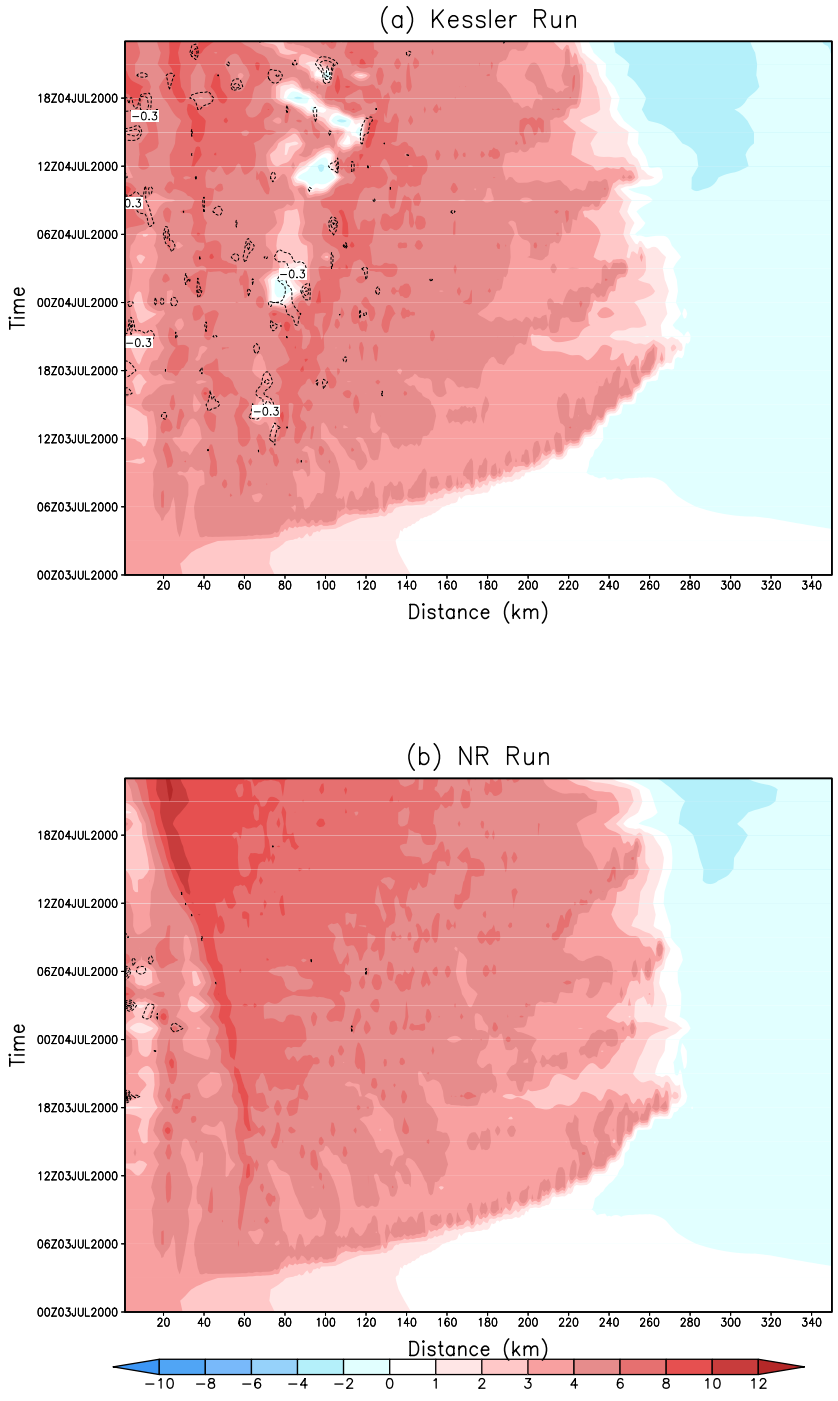

Figure 3.6: Time histories of minimum SLP in several experiments K, NCR and NR

cloud droplets, both of which were absent in NCR, but still reaches its tipping point earlier than the control run.

3.3 Surface heat flux

In the WISHE mechanism, the surface heat flux plays an important role in intensifying a weak vortex. Figure 3.8 shows the total surface heat flux for the K, NR and NCR storms. All three simulations commence with a flux of about 100 W/m^2 as they are initialized with the same relatively weak vortex. It is noticed that all the TCs reach 300 W/m^2 around the time that RI starts, and heat fluxes remain large beneath the eyewall for the balance of the simulation. This suggests that there may be a critical surface heat flux value that is needed to trigger RI.

To test this, another NCR simulation is made in which the total surface heat flux is restricted to be $\leq$ 100 W/m^2 for radii r $\leq$ 100 km from very start (Figure 3.9). Figure 3.9a shows that limiting the total surface heat flux can decrease TCs maximum intensity relative to the original storm but has little effect on the RI onset time. Both simulations reach the RI stage around 12 h, and keep intensifying for 2 days before reaching a steady state at around the same time. This surface heat flux manipulation does not change the RI onset time in the control or NR cases either (not shown).

Although restricting the surface heat flux is not found to delay the RI onset time, we see we can hasten organization by forcing the flux to be larger in the core region. We will demonstrate this with the control K microphysics. In Figure 3.10, the perturbation θ_e and vertical velocity fields at 18 h are shown for the control run and a simulation we will call K-gt500-core in which the total surface heat flux is at least 500 W/m^2 for the radial range of 10 $\leq$ r $\leq$ 80 km from the start. At this time, the K simulation (Figure 3.10a) has a deep updraft at r = 70 km that will be short-lived as the active convection out past 100 km from the center continues to develop. In contrast, the K-gt500-core

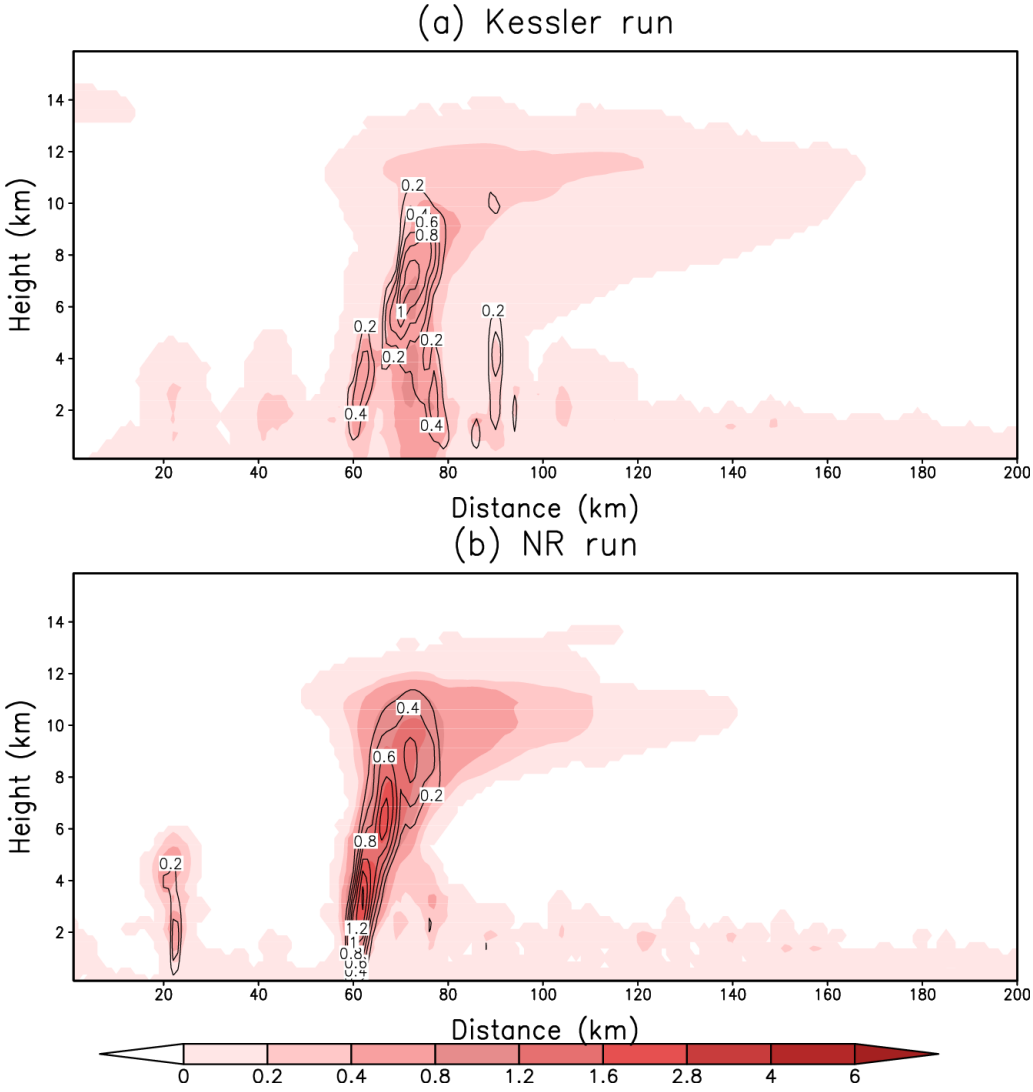

Figure 3.7: Total liquid water content (color field) and vertical velocity (contour) average from 10 h to 20 h for (a) Control, and (b) NR.

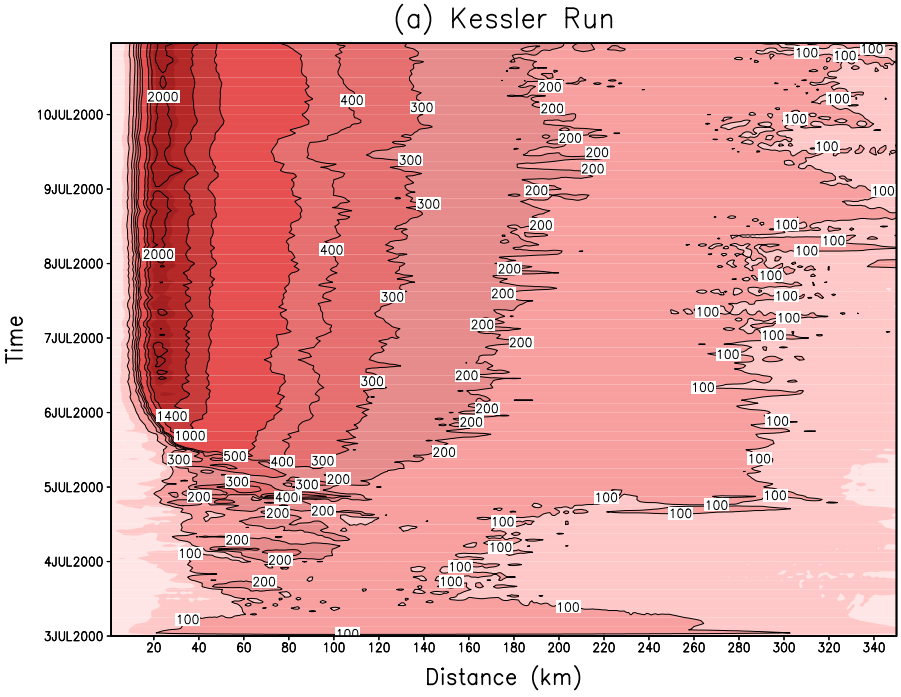
(a) Kessler Run
Time
10JUL2000
9JUL2000
8JUL2000
7JUL2000
6JUL2000
5JUL2000
4JUL2000
3JUL2000
20 40 60 80 100 120 140 160 180 200 220 240 260 280 300 320 340
Distance (km)

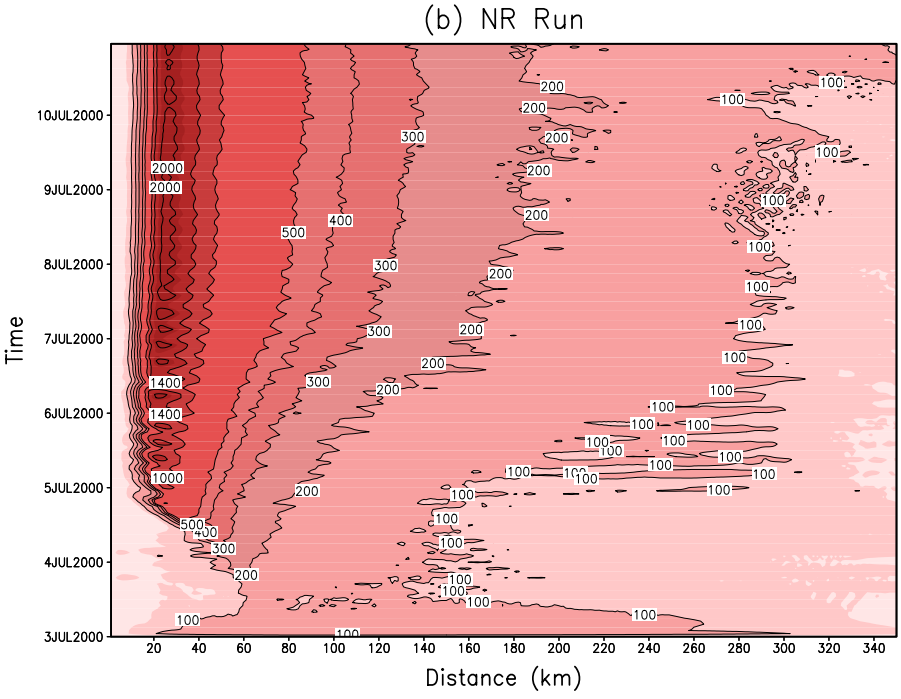
(b) NR Run
Time
10JUL2000
9JUL2000
8JUL2000
7JUL2000
6JUL2000
5JUL2000
4JUL2000
3JUL2000
20 40 60 80 100 120 140 160 180 200 220 240 260 280 300 320 340
Distance (km)

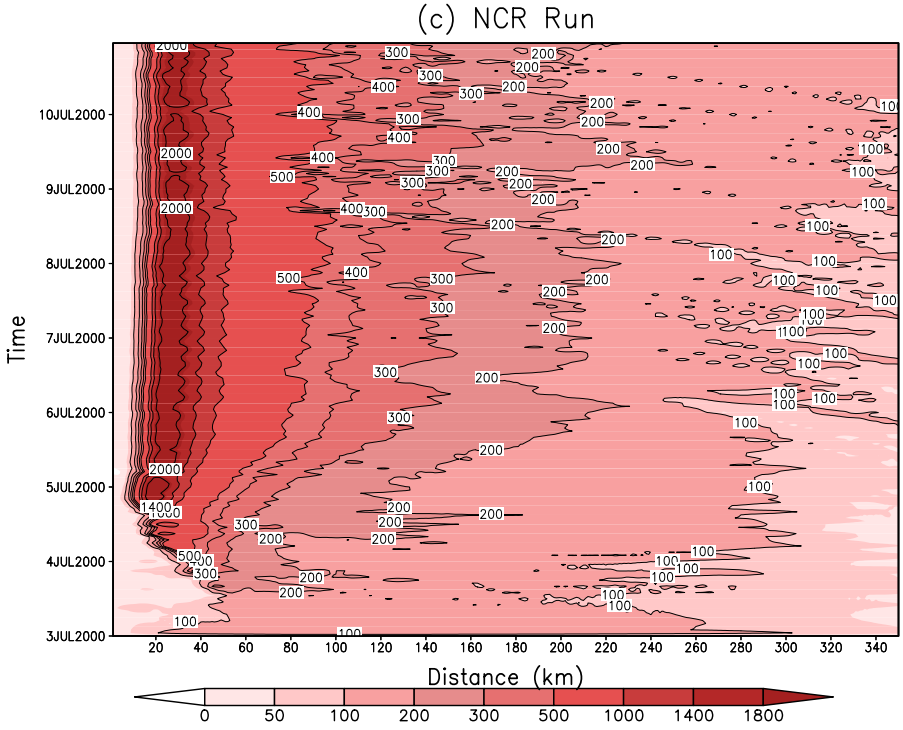

Figure 3.8: Hovmoller diagrams of total surface heat flux (W/m^2) for K, NR and NCR

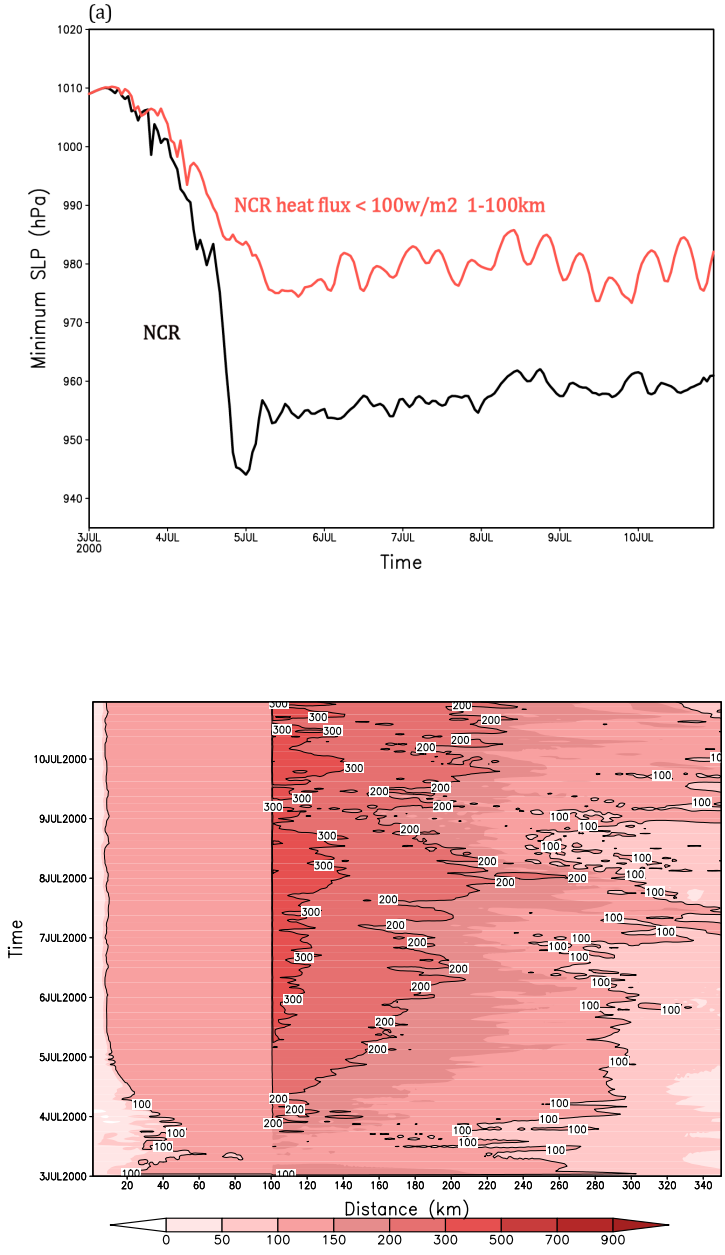

Figure 3.9: (a) Time histories of minimum SLP for NCR simulations with the original and modified surface heat fluxes; (b) Hovmoller diagram of the total surface heat flux (W/m^2) in the modified NCR run (colored and contoured).

storm (Figure 3.10) is already organized with a strong, well-developed eyewall updraft at r = 20 km. Minor convection at r = 80 km will fail to develop further. The time history of the K-gt500-core storms minimum SLP (Figure 3.11) closely resembles that of the NCR case (Figure 3.5), heretofore our most rapidly organizing TC.

However, there is not a simple relationship between the magnitude of the total surface heat flux and the RI onset time, as illustrated by three additional simulations. For cases K-gt200-core, K-gt300-core and K-gt400-core, the total surface heat flux in the $10 \leq r \leq 80$ km radial range is restricted to be $\geq$ 200, 300 and 400 W/m^2 from the start, respectively. Figure 3.12 shows that the tipping points of the K-gt200-core, K-gt300-core and K-gt400-core storms occur almost at the same time, about 1.5 days earlier than the control run, but 20 h slower than for K-gt200-core. These results suggest two thresholds exist, around 200 and between 400-500 W/m^2 for early and very early RI onset, respectively. Once RI begins, however, the rate of development is about the same in all of the cases shown, including the control run.

3.4 Influence of convective activity

So, we have seen that decreasing the surface heat flux does not delay the onset of organization although increasing the surface heat flux can hasten it. It seems that the surface heat flux is not the most direct factor determining the tipping point. Thus, we now turn to considering the potential influence of convective activity near what eventually becomes the storm inner core region, as differences in convective activity between the K and K-gt500-core runs can be noted even very early in the simulations. For example, at 7 h, the K-gt500-core storm already has developing deep convection occurring inward of r = 80 km (Figure 3.13a), while in the control run there is only shallower activity spread over a wider range (Figure 3.13b).

Storms K and K-gt500-core will now be compared to two additional simulations,

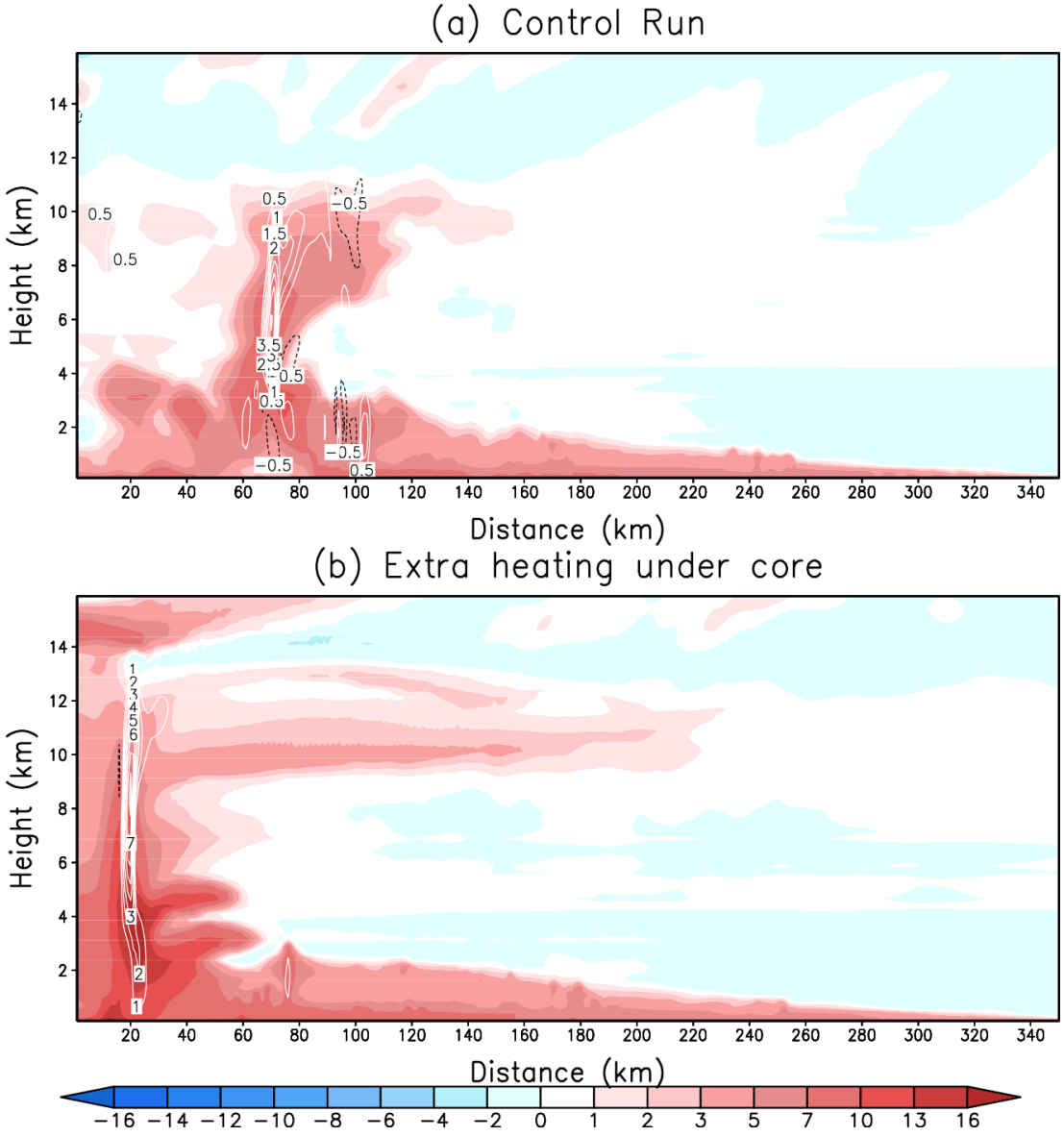

Figure 3.10: θ_e perturbation (color field) and upward (white contours) and downward (black contours) vertical velocity fields at 18 h for (a) K (control run); (b) a simulation with surface heat flux ≥ 500 W/m^2 between r = 10-80 km.

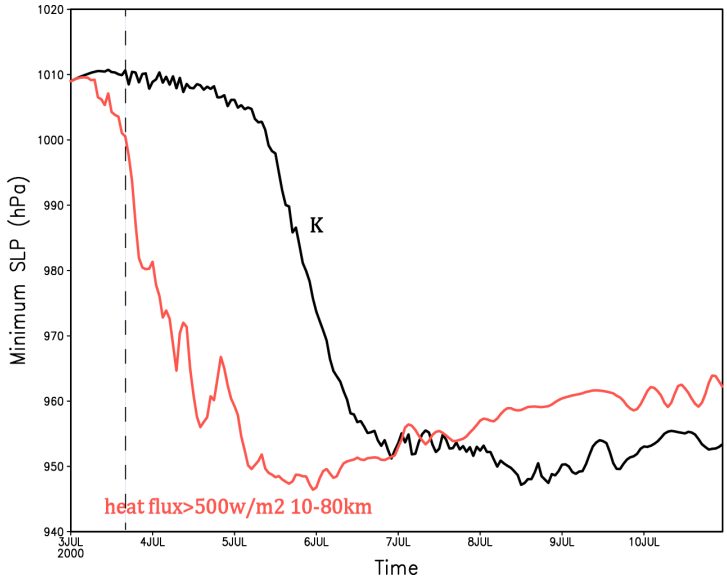

Figure 3.11: Time histories of minimum SLP for the control Kessler (black) and K-gt500-core (red) storms.

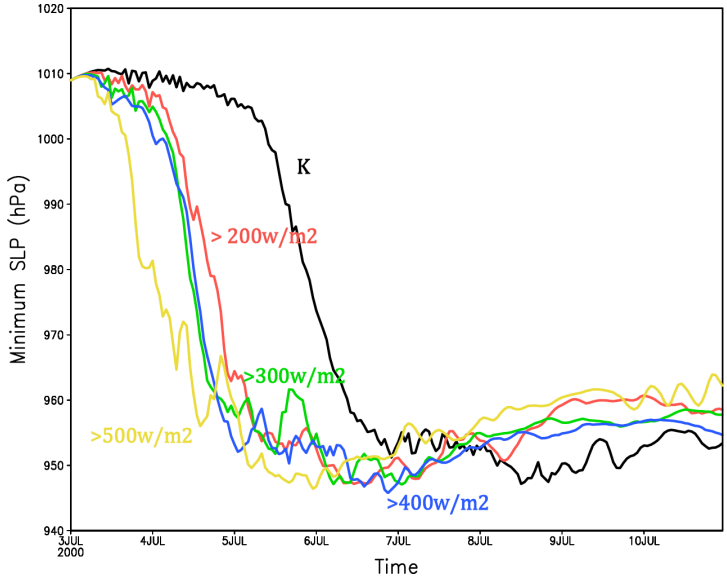

Figure 3.12: Time histories of minimum SLP from the Kessler (black), K-gt200-core (red), K-gt300-core (green), K-gt400-core (blue) and K-gt500-core (yellow) simulations.

designed to assess the influence of convective activity on the tipping point. The third simulation, called K-bubbles-7hr (Figure 3.13c), is created by restarting K at 7 h, but with some warm, moist bubbles added to mimic the pattern of convection seen in the K-gt500-core run at this time. The bubbles are positioned at r = 40 and 70 km, corresponding to the locations of the more active updrafts in the K-gt500-core storm, but in the lower troposphere so they can develop into their own convective cells. The fourth simulation, called K-gt500-7h, is like K-gt500-core, but the heat flux restriction is removed after 7 h, permitting the flux to return to its natural state, determined solely by horizontal wind speeds and vertical gradients (Figure 3.15).

Figure 3.14 reveals that the K-gt500-7hr and K-bubbles-7hr storms commence RI at almost the same time (Figure 3.14), much faster than the control K run although less quickly than in the K-gt500-core simulation. Taken together, the K-gt500-7hr and K-bubbles-7hr runs suggest that once deep convection in the inner core region starts, storm organization will continue until the tipping point is reached. The difference between them and K, is that the control run is unable to achieve inner core strong convective activity so quickly without an at least temporary heat flux enhancement or a boost from the insertion of buoyant bubbles. Therefore, the direct effect on the tipping point appears to be inner core convective activity.

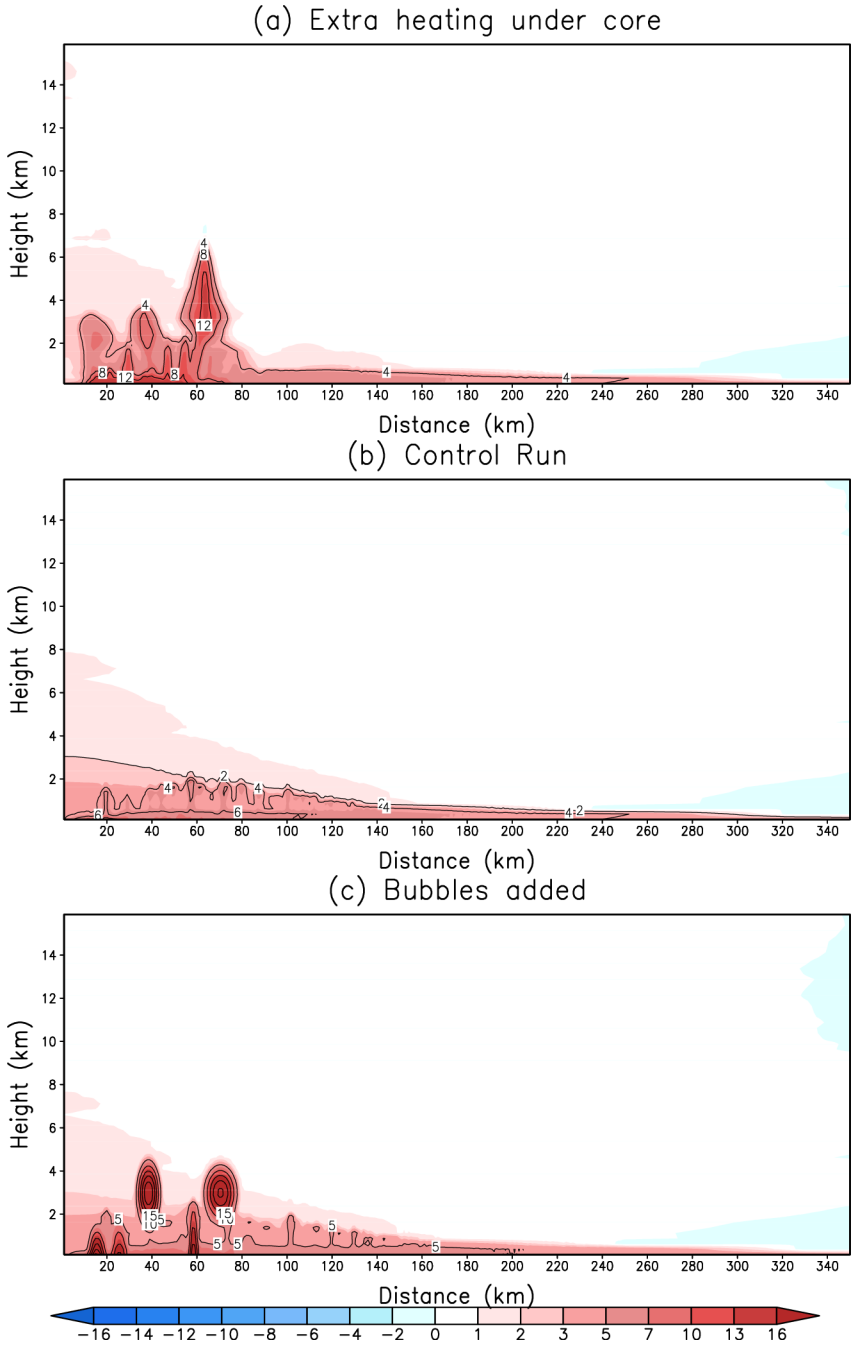

Figure 3.13: θ_e perturbation (color field and black contours) in experiments at 7 h with (a) total surface heat flux forced to be greater than 500w/m^2 (K-gt500-core run); (b) K (control run); (c) control run with bubbles added at 7 h (K-bubbles-7hr run)

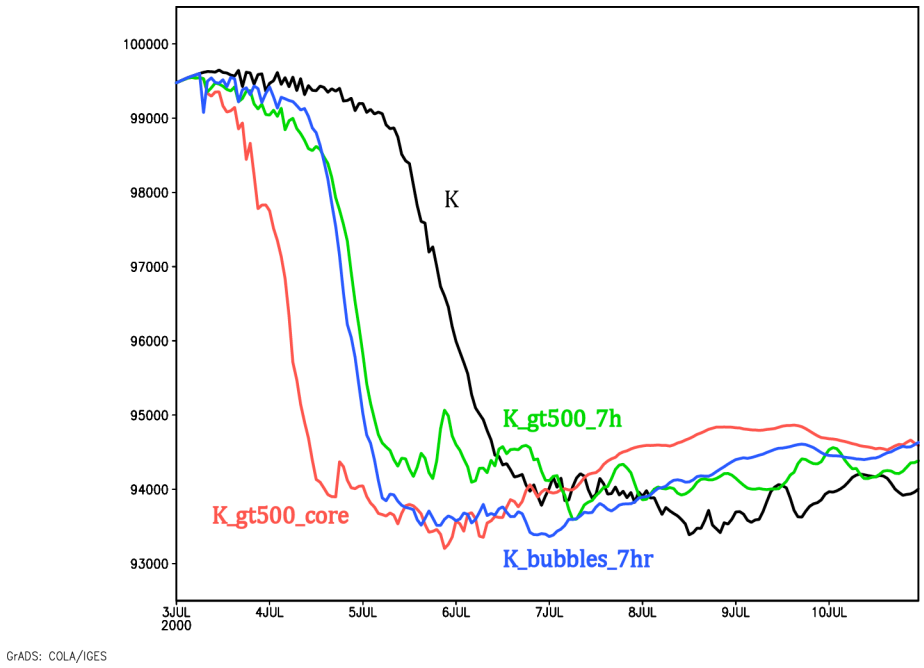

Figure 3.14: Time histories of minimum SLP of control run (black), K-gt500-core run (red), K-gt500-7hr run (green), K-bubbles-7hr run (blue)

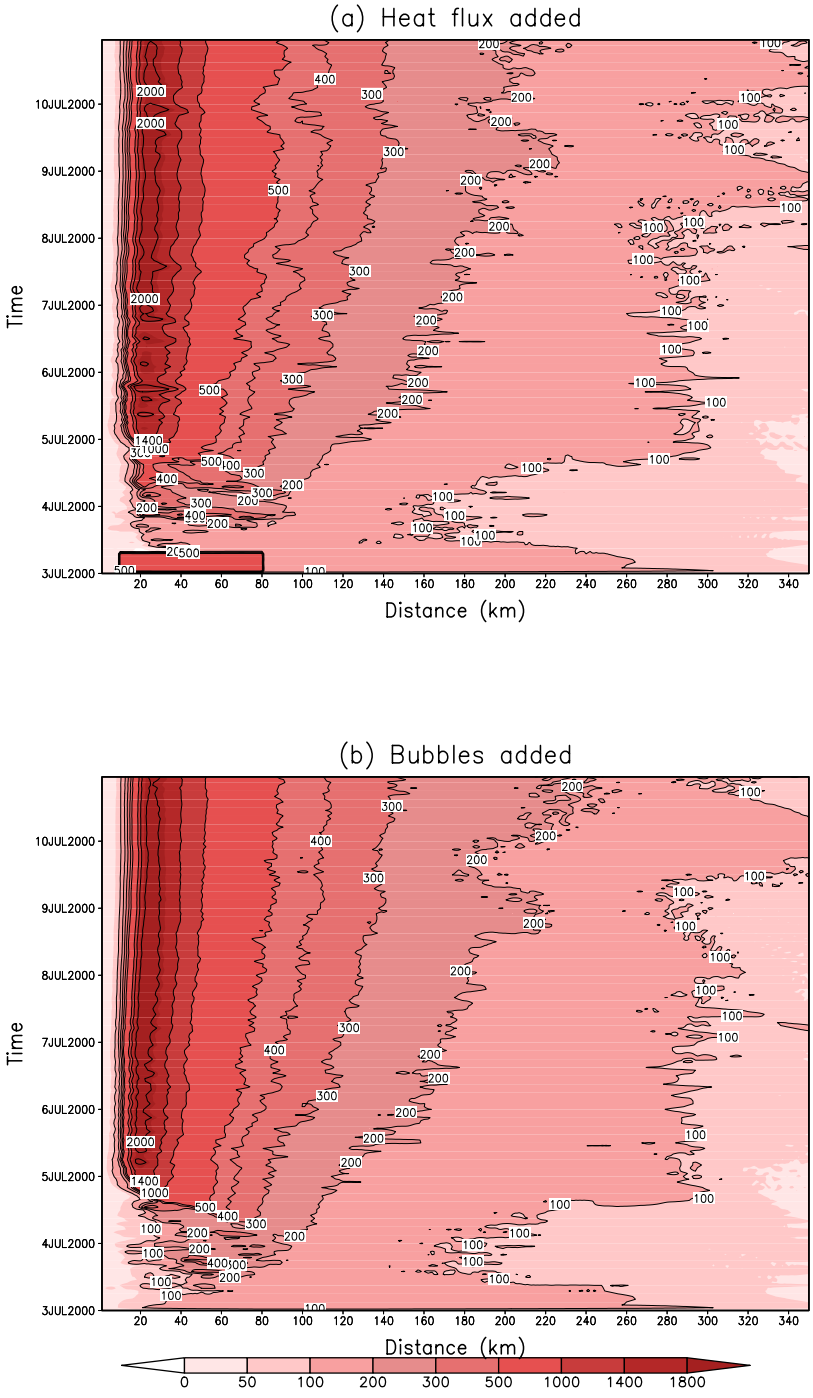

Figure 3.15: Hovmoller diagram of total surface heat flux (color field and contours) for experiments (a) K-gt500-7hr run; and (b) K-bubbles-7hr

CHAPTER 4

Two factors

Based on the simulations in Chapter 3 and an analysis of the common features that are always met before the tipping point is reached, we propose that there are two necessary factors that need to be satisfied prior to RI onset. One is achieving an approximately moist adiabatic profile within the core. The other is elimination of significant convection at outer radii via suppression or merger with convection in the inner region.

4.1 Vertical θ_e profile in the core region

Figure 4.1 shows the vertical θ_e profile averaged between 1 and 50 km from the center at three different times for the K, Rotunno and NCR model storms. Each shows a temporal progression towards a moist adiabatic profile through much of the troposphere, primarily by raising the θ_e of the middle and upper troposphere. This occurs fastest in the NCR run which is also the first one to achieve RI among these three simulations (Figure 3.5). Thus, we hypothesize that moist adiabatic is a necessary condition for RI occurrence.

To test this assumption, we initialize a simulation with a vertical sounding that is already moist adiabatic beneath the tropopause (Figure 4.2a). We call this simulation the constant-θ_e run, referencing its tropospheric thermodynamic structure. Initial temperature and vapor content are the same at surface for these two soundings, but mid-tropospheric θ_e is about 10 K higher in the moist adiabatic profile. Figure 4.2b shows the initial profile change has a smaller impact on final strength and intensifi-

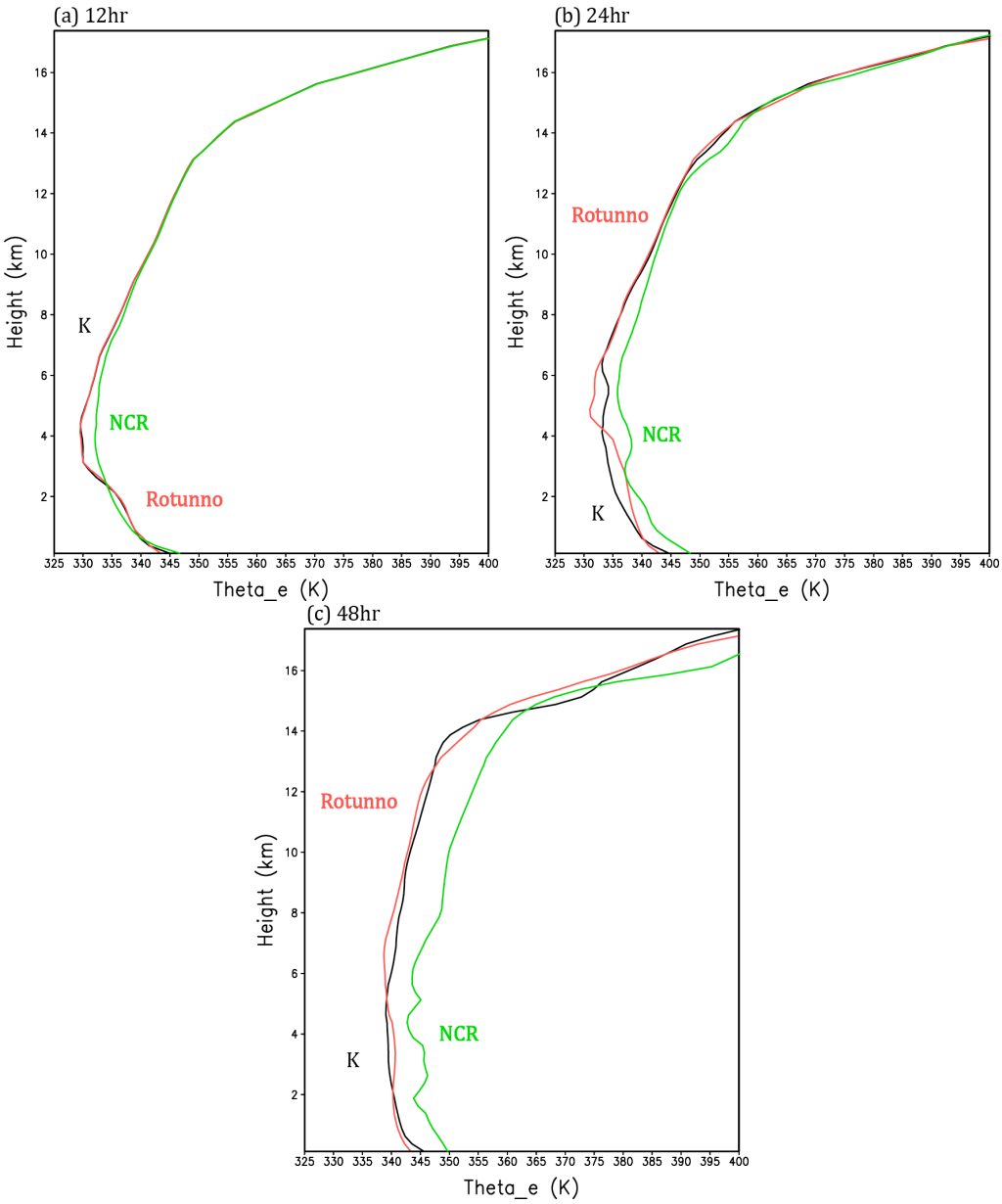

Figure 4.1: Vertical profiles of θ_e averaged in the $1 \leq r \leq 50$ km radial range for the Kessler (black), Rotunno (red) and NCR (green) simulations at (a) 12 h, (b) 24 h, and (c) 48 h.

cation rate during the RI period than it has on the timing of the tipping point. The constant-θ_e runs gestation period is shorter by 1.5 days. Although we cannot conclude that it is a necessary condition for RI at this point, it is obvious that a moist adiabatic profile is a positive factor contributing to the timing of RI.

While the Kessler and Rotunno runs achieve moist adiabatic profiles at about the same time (Figure 4.1), and before their RI onsets, we saw earlier that the tipping point was reached about 10 h earlier with Kessler microphysics (Figure 3.4). Thus, it is possible that other factors also control the process. Figure 4.3 presents Hovmoller diagrams of θ_e at the 4 km level for these two simulations. In both, convective activity is seen propagating outward in the first 48 h, then moving inward. Their eyewalls do not form until convection beyond a radius of 80 km or so is either suppressed or manages to move farther inward. The later-onset Rotunno run appears to have more widespread and persistent convective activity. Therefore, it is hypothesized that outer convection makes the difference in tipping points between this pair of storms.

Figure 4.4 shows θ_e profiles from the K, NCR and Rotunno runs, averaged between radii of 120 km and 200 km, which we will consider the outer region. In contrast to the inner core profiles (Figure 4.1), midtropospheric θ_e remains low in the NCR and K runs, but becomes higher in the Rotunno storm by 54 h (Figure 4.1d), reflecting the greater convective activity in that radial range. Beyond this time, the Rotunno TCs midtropospheric θ_e starts decreasing (not shown) and all simulations eventually develop even lower values in that layer than they started with as convective activity becomes concentrated in the storm inner core. It is possible that suppressing convective activity earlier favors RI and the inability of the Rotunno MP to accomplish this as quickly accounts for its delayed tipping point. This is explored in the next section.

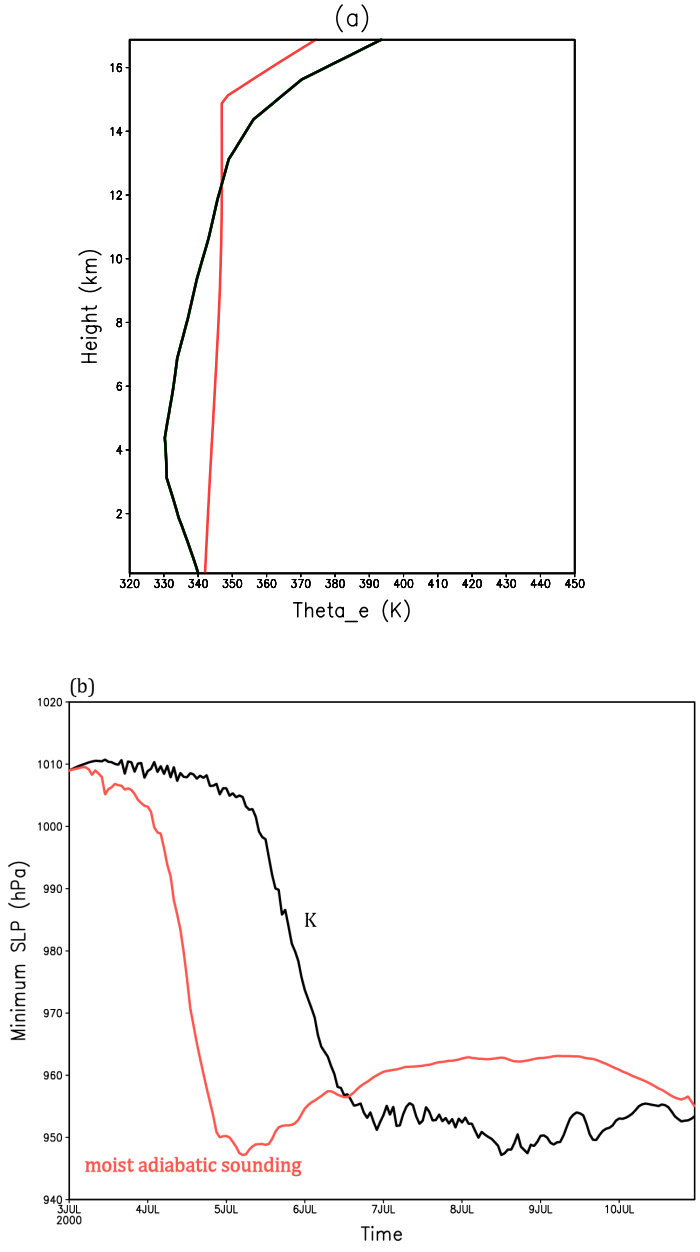

Figure 4.2: (a) Vertical θ_e profiles at initial time. (b) Time histories of minimum SLP in these experiments

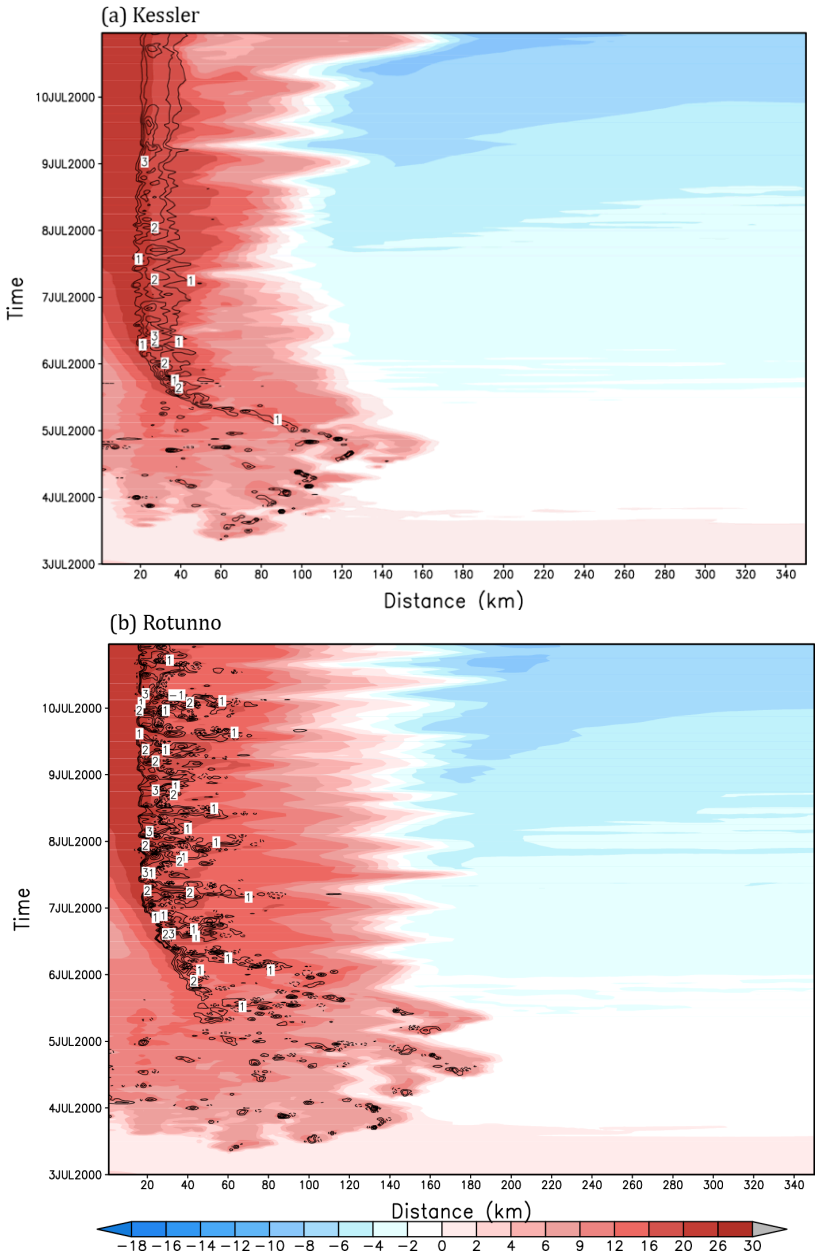

Figure 4.3: θ_e (color field) and upward velocity (contours) of (a) Kessler and (b) Rotunno at 4 km height

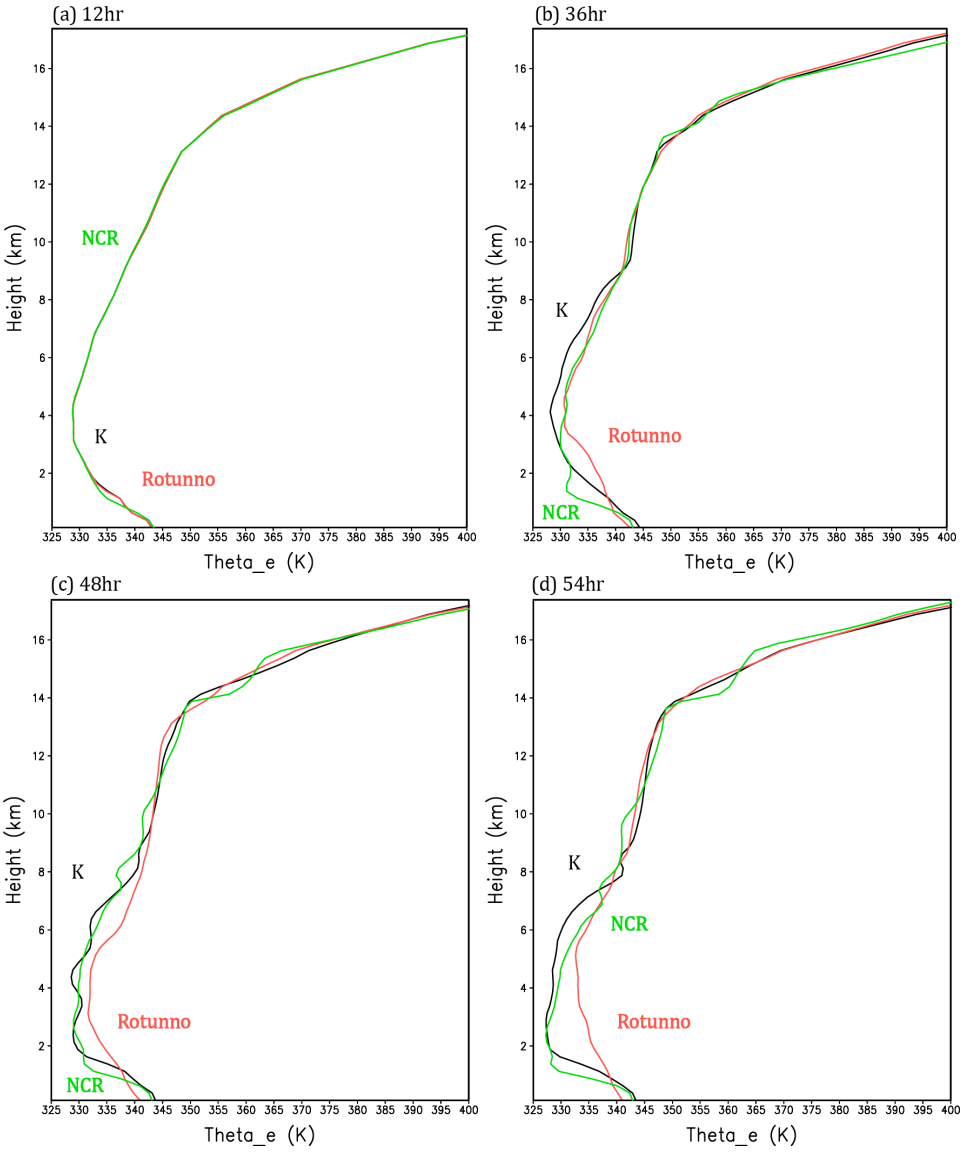

Figure 4.4: Vertical profiles of θ_e averaged through the $120 \leq r \leq 200$ km radial range for the Kessler (black), Rotunno (red) and NCR (green) model storms at (a) 18 h, (b) 36 h, (c) 48 h, and (d) 54 h.

4.2 Convection at outer radii

It is possible that strong peripheral convective activity has to be suppressed before RI can proceed because it disrupts the inflow of angular momentum and water vapor towards the storm core. To examine this surmise, a K-based simulation named K-gt300-outer is carried out. In this run, the total surface heat flux is restricted to be $\geq$ 300 W/m^2 for radii between 200 and 350 km from the center. This represents an enhancement to the heat flux seen in the control run in this radial band (see Figure 3.8a).

By 18 h, the extra heat flux in the K-gt300-outer case is inducing strong overturning motions around r = 240 km, which is not only more intense than the activity anywhere else at this time, but also shifted significantly farther outward than the convection seen in the K storm (Figure 4.5). The enhanced outer convection delays the tipping point by 1.5 days relative to the control. Once RI starts, K-gt300-out and K have the same deepening rate, although the flux enhancement results in a weaker final intensity. This pair of simulations suggests that the increased outer convective activity can indeed delay the tipping point, as surmised.

As mentioned in Chapter 1, *Braun et al.* (2012)'s results indicate that the dry air at mid-level has a negative impact on the development of TCs, delaying the tipping point, no matter how far away the dry air is displaced from the storm center (see Figure 1.3). It seems that although the dry air layer can suppress convection in the outer region, that does not mean the tipping point has to occur earlier. *Braun et al.* (2012) suggest that the intrusion of the dry air delays of the intensification of the TC mainly via causing the storm circulation and diabatic heating azimuthally asymmetric. This appears to contradict the foregoing results.

To explore this, we now conduct two simulations similar to the *Braun et al.* (2012) situation but using this axisymmetric model to explore how the dry tongue by itself in-

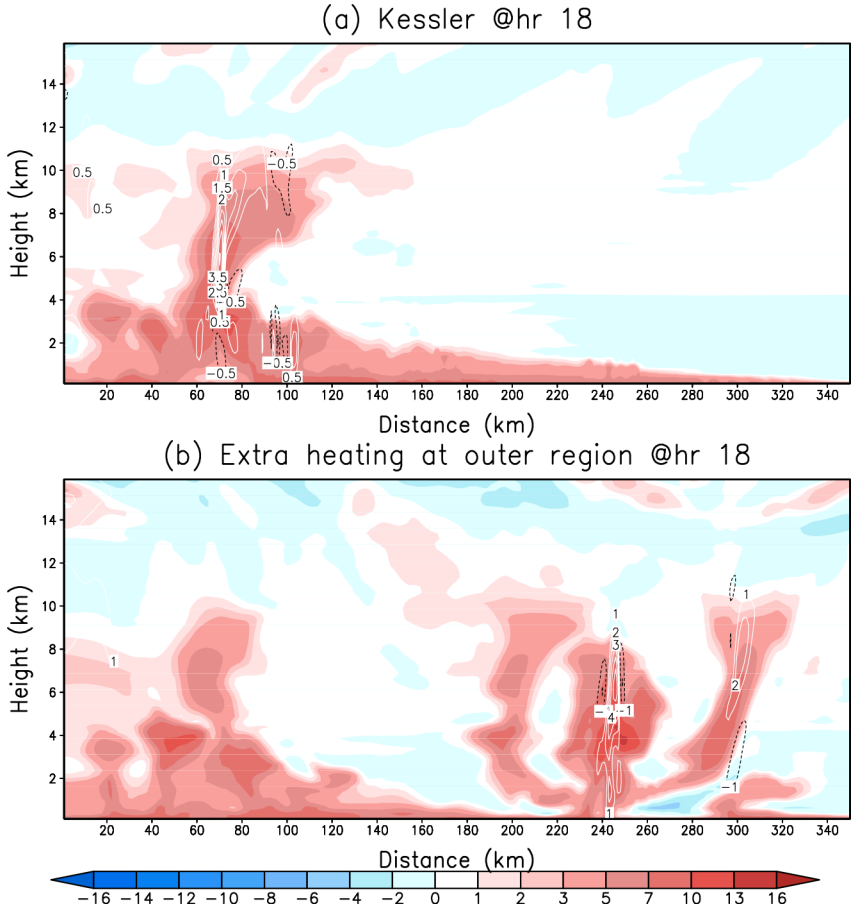

Figure 4.5: θ_e (colored) and upward (white contours) and downward (black contours) vertical velocity fields at hour 18 for (a) K (control run); and (b) K-gt300-outer run (300 W/m^2 between 200-350km)

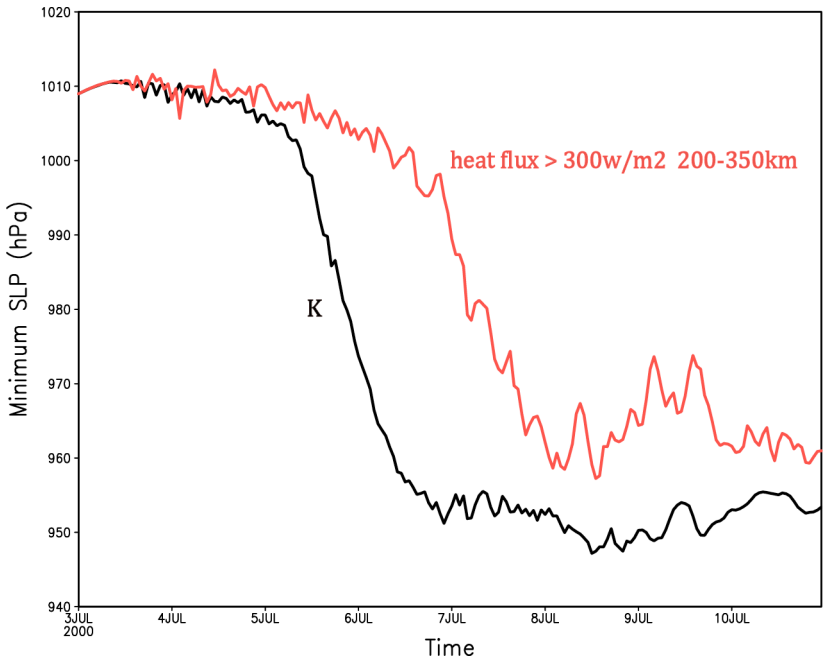

Figure 4.6: Time histories of minimum SLP from the Kessler (black) and K-gt300-outer (red) simulations.

fluences the TC development. (By its nature, the axisymmetric model does not permit azimuthal asymmetries, so the potential weakening mechanism identified by *Braun et al.* (2012) does not exist.) These simulations are initialized with dry tongues occupying the 3-6 km layer in the vertical that start at a particular radius r, and extend across the domain. One such tongues inward edge is initially placed at 90 km, so the dry air originally occupies radii $\geq$ 90 km, and the other starts at 120km (i.e., r $\geq$ 120 km). Figure 4.7 is an example of initial condition in the r $\geq$ 90 km run. The θ_e is relatively low in the 3-6 km layer owing to the moisture reduction.

Figure 4.8 shows again the time histories of minimum SLP for the control and NCR storms, now joined by the two dry tongue runs. Note that the TC of r $\geq$ 90 km run develops a little later than control run but the tipping point for the r $\geq$ 120 km case is about 30 h earlier. Still, they have the same intensification rate beyond the tipping point, and achieve similar final intensities.

Animation of these dry tongue simulations (not shown here) demonstrates that the

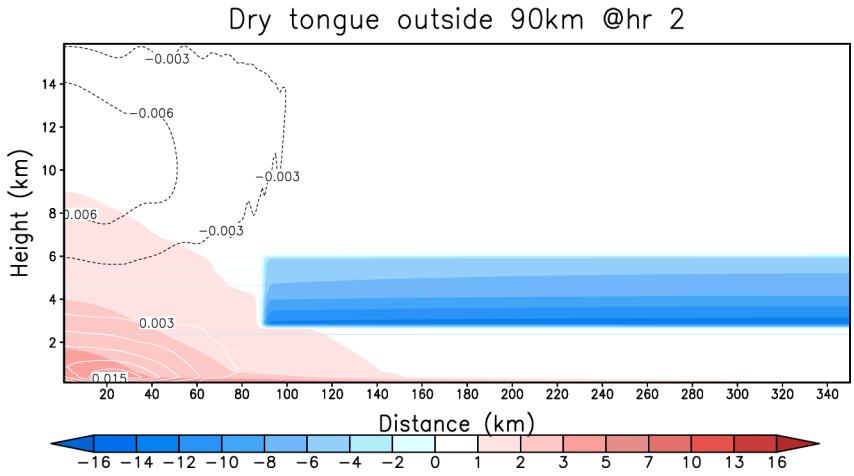

Figure 4.7: Initial condition from the r ≥ 90 km run. Shown is θ_e difference from the tongueless (control) initial condition (colored).

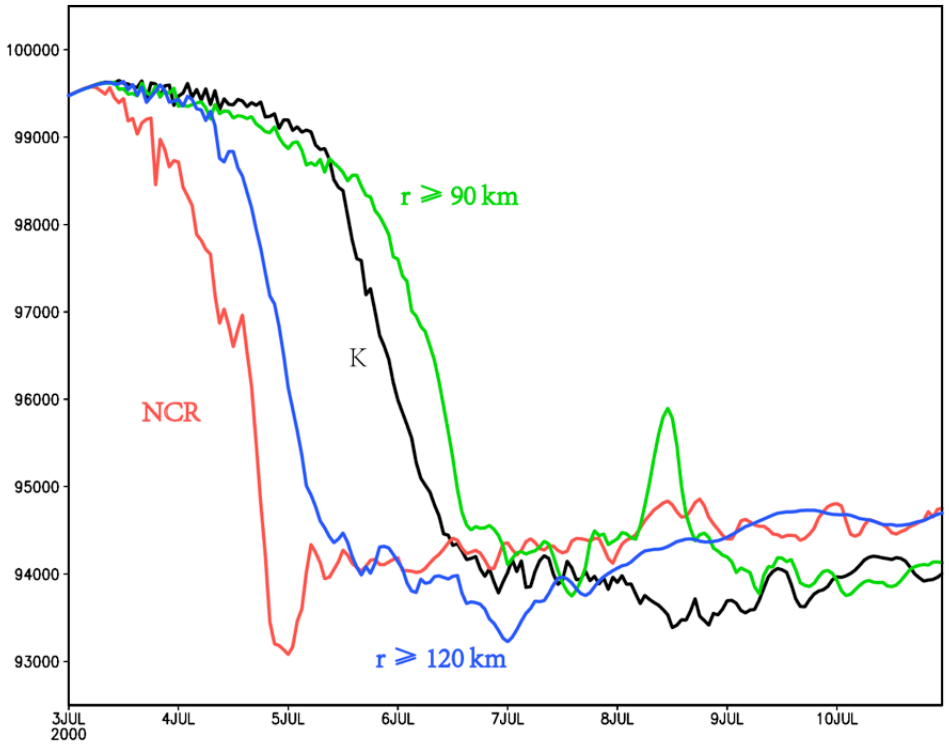

Figure 4.8: Time histories of minimum SLP for the control (black), NCR (red), and two dry tongue runs: r ≥ 90 km (green) and r ≥ 120 km (blue).

dry layers effectively suppress deep convection beneath them. However, the inward position (head) of the tongue can shift over time, in response to convection closer to the core and the developing secondary (radial) circulation. In the r ≥ 90 km storm, for example, the head of the dry tongue becomes moistened by the development of inner core convection, which makes it appear that the tongue is continuously pushed outward (which is accompanied by the outward extension of the inner convection). By 26 h, the dry tongue of the r ≥ 90 km run retreats to 100 km (Figure 4.9a). Another 17 h later, the head is found at 110 km (Figure 4.10b) and thus can only suppress the convection outside that radius.

Although the tongue in this case is shifting radially outward, it remains close to the RMW, and Figures 4.9a, b illustrate that the dry air can be easily transported or mixed into the inner core, delaying the storm organization. Note that low θ_e air from the dry tongue can be seen to start penetrating the root of a deep convective cell (near r = 80 km in Figure 4.9a), a consequence of a transient downdraft. One hour later, this dry air intrusion has been isolated from the dry tongue by the development of new convection at 90 km (Figure 4.9b). However, note has also progressed inward as far as r = 40 km, increasing the stability in the inner core region and weakening the updraft there.

The situation is different in the r ≥ 120 km case. The dry tongue starts farther from the initial RMW, so tongue air does not enter the inner core to disrupt the ascent there or become moistened (Figures 4.9c, d). Yet, it still acts to suppress convective activity at outer radii. Note the r ≥ 120 km cases dry tongue shifts progressively farther inward with time, its head reaching 100 km at 26 h (Figure 4.9d) and 60 km by 43 h (Figure 4.10a).

Figure 4.10 clearly shows that the TC contracts and strengthens fastest in the r ≥ 120 km run. This storm (Figure 4.10a) possesses a well-developed eyewall updraft around r = 25 km and there is no deep convection farther outward. In the r ≥ 90 km run (Figure 4.10b), we see an eyewall present around r = 40 km, but another

development is in progress very close to the dry tongues head that will compete with the inner core organization, disrupting TC organization. The control run (Figure 4.10c) appears least organized at this time and has convective activity extending as far as r = 160 km. However, lacking a significant dry tongue, it is not subjected to periodic ingestions of dry air. It is possible that the weakened inner core convection in the r $\geq$ 90 km case owing to the dry intrusions cancels out the benefit the suppression of outer convective activity, which permits the ostensibly less well-organized control run to reach its tipping point first (as was shown in Figure 4.8.)

These simulations suggest that the tipping point is sensitive to the initial relative location of the RMW and the dry tongue. The optimal positioning of the head should satisfy two conditions: one is to keep a safe distance from the maximum wind; the other is to suppress convection beyond the inner core, which can disrupt the development of the secondary circulation. If the dry tongue is too far away, it fails to prevent the appearance of peripheral convection that may compete with the organization of the inner core. However, if the dry tongue comes too close to the initial RMW, the storm can experience weakening owing to dry air injections.

To verify the delayed RI is resulted from the competition between the inner core and the peripheral convection, a simulation called K-heatlt50 is performed, which attempts to suppress the outer radius convection without encouraging too much low-θ_e air to become injected into the inner core region. This is done by limiting the total surface heat flux to be less than 50 W/m^2 beyond the radius of 90 km (Figure 4.11). This storm enters the RI stage about 1 day earlier than the control run and 1.5 days earlier than the dry tongue run (Figure 4.12). Animations (not shown) reveal the control run has more peripheral convection than either the K-heatlt50 or the r $\geq$ 90 km dry tongue runs. As for the inner core region, the eyewall organizes fastest in the K-heatlt50 run and slowest in the dry tongue run, which experiences periodic dry intrusions. This appears to demonstrate that, by itself, suppressing peripheral convection

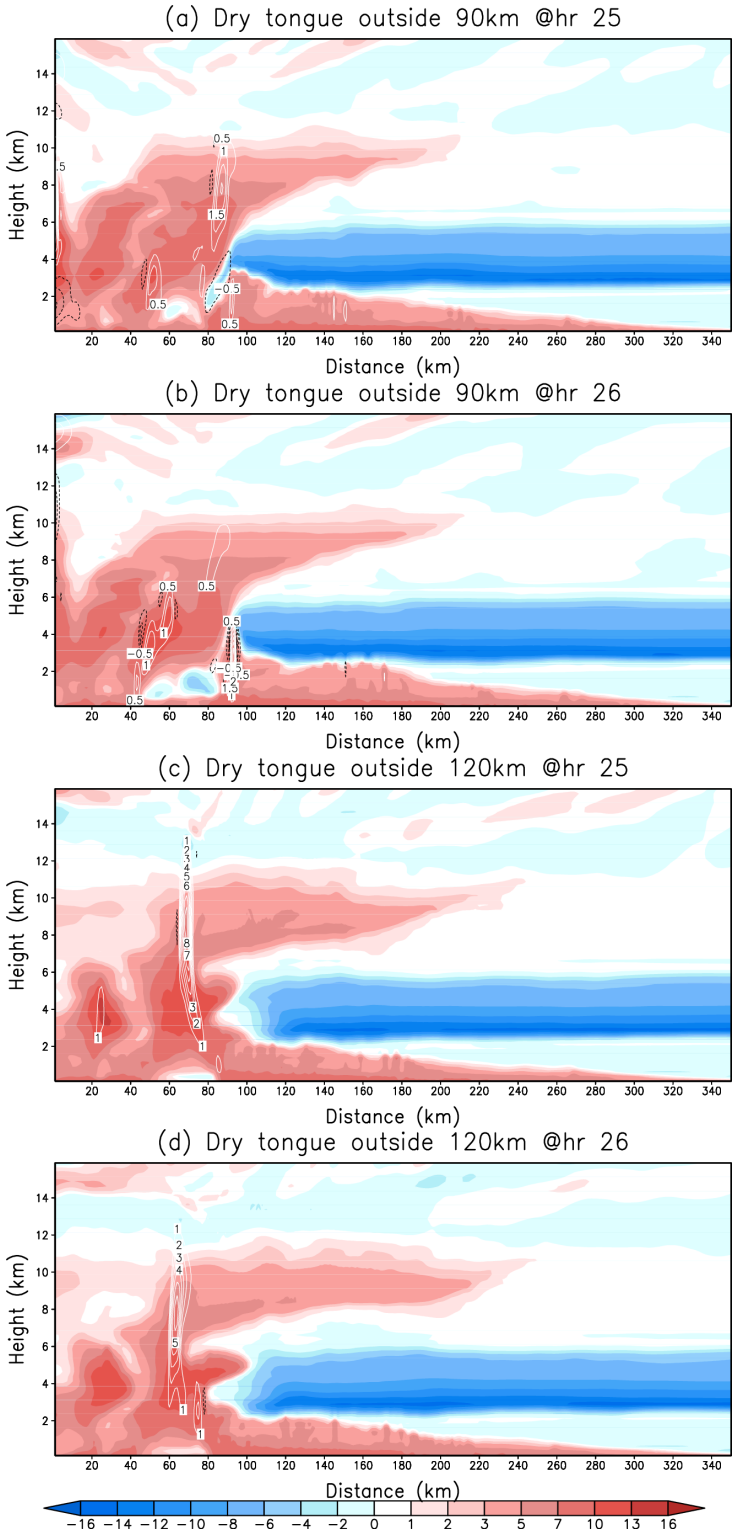

Figure 4.9: Plots of θ_e perturbation, computed relative to the initial condition of the tongueless or control run, and vertical velocity (as in Figure 4.5) for the (a) r ≥ 90 km case at 25 h, (b) r ≥ 90 km case at 26 h, (c) r ≥ 120 km storm at 25 h and (d) r ≥ 120 km storm at 26 h.

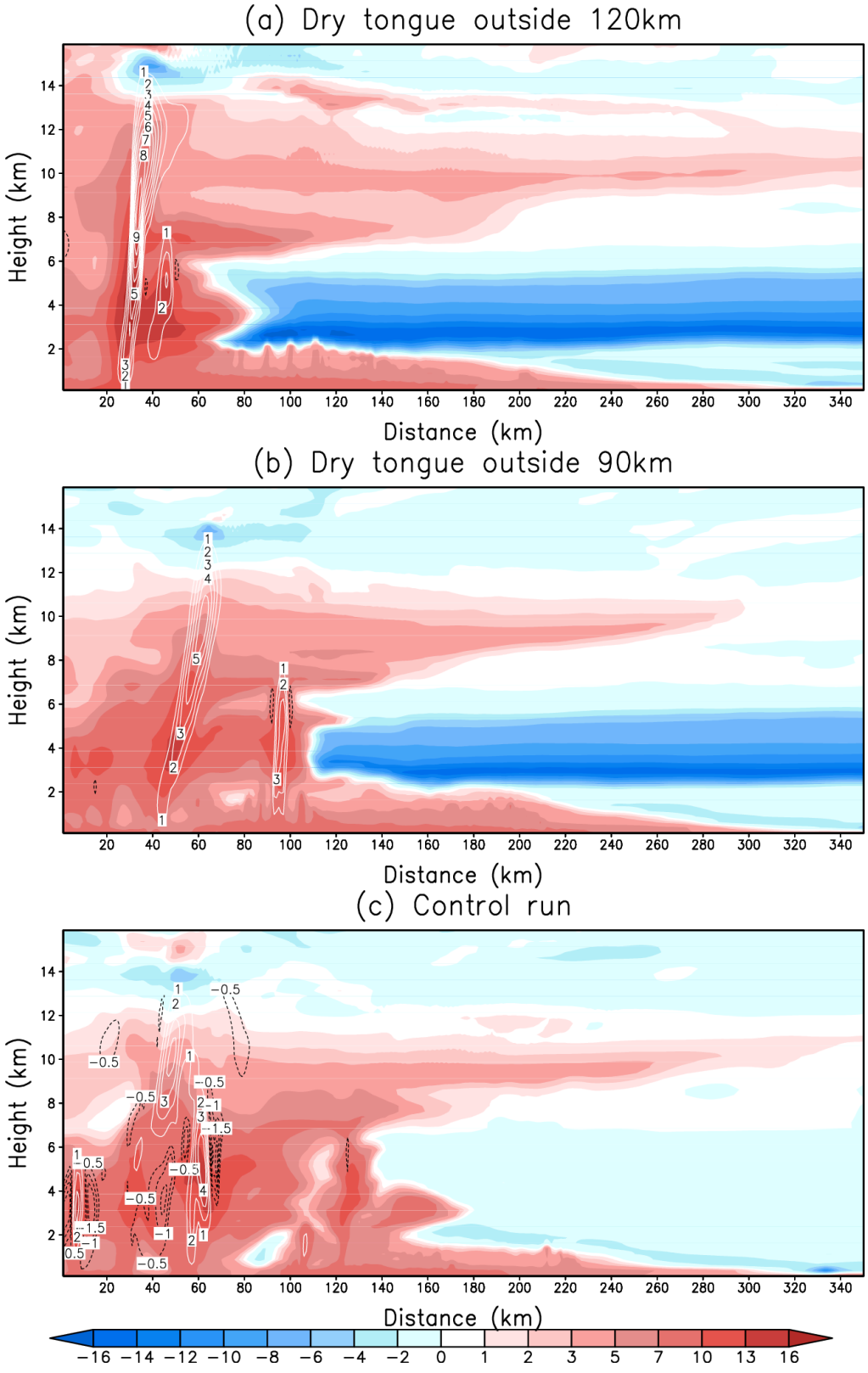

Figure 4.10: As in Figure 4.9, but at 43 h, for the (a) r ≥ 120 km, (b) r ≥ 90 km, (c) control run

can hasten storm organization, but this positive effect can be mitigated if entrainment of convectively unfavorable air also occurs.

Figure 4.13 presents Hovmoller diagrams of perturbation θ_e at 2.75 km altitude. Without any external mechanism to suppress the outer convection, the control run possesses high θ_e values extending to 180 km (Figure 4.13a), which is farther outward than in the dry tongue and k-heatlt50 cases. At 30 h, an inner eye wall forms at r = 24 km, but convective activity develops at r = 140 km at the same time. This outer convection strengthens as it moves inward, apparently disrupting the ability of the control run to organize an inner core eyewall. Before the tipping point in the dry tongue case (Figure 4.13c), there is some convective activity extending out to r = 100 km several hours after the formation of an eyewall at r = 50 km.

In those two cases, the eyewalls do not intensify or become steady until the peripheral convection has successfully merges inward or is suppressed. In the K-heatlt50 run, only one major eyewall forms at 26 h. There is no strong outer convection to interrupt or delay the organizational process. Around 45 h, the concentration of convection in the core of the storm and the onset of RI occur simultaneously. These results suggest that the inner core convection cannot become, or remain, strong until the peripheral activity disappears.

4.3 How does peripheral convection influence the tipping point?

According to *Smith et al.* (2009), the convergence of the absolute angular momentum (AAM) within the boundary layer is very important for the vortex spin-up process. AAM generally increases outward from the center, owing to its dependence on radius, and can be transported inward by the secondary circulation in the lower troposphere. The tangential wind speed will increase where and when the isopleths of mean AAM move inward. We now consider the influence of the peripheral convective activity in

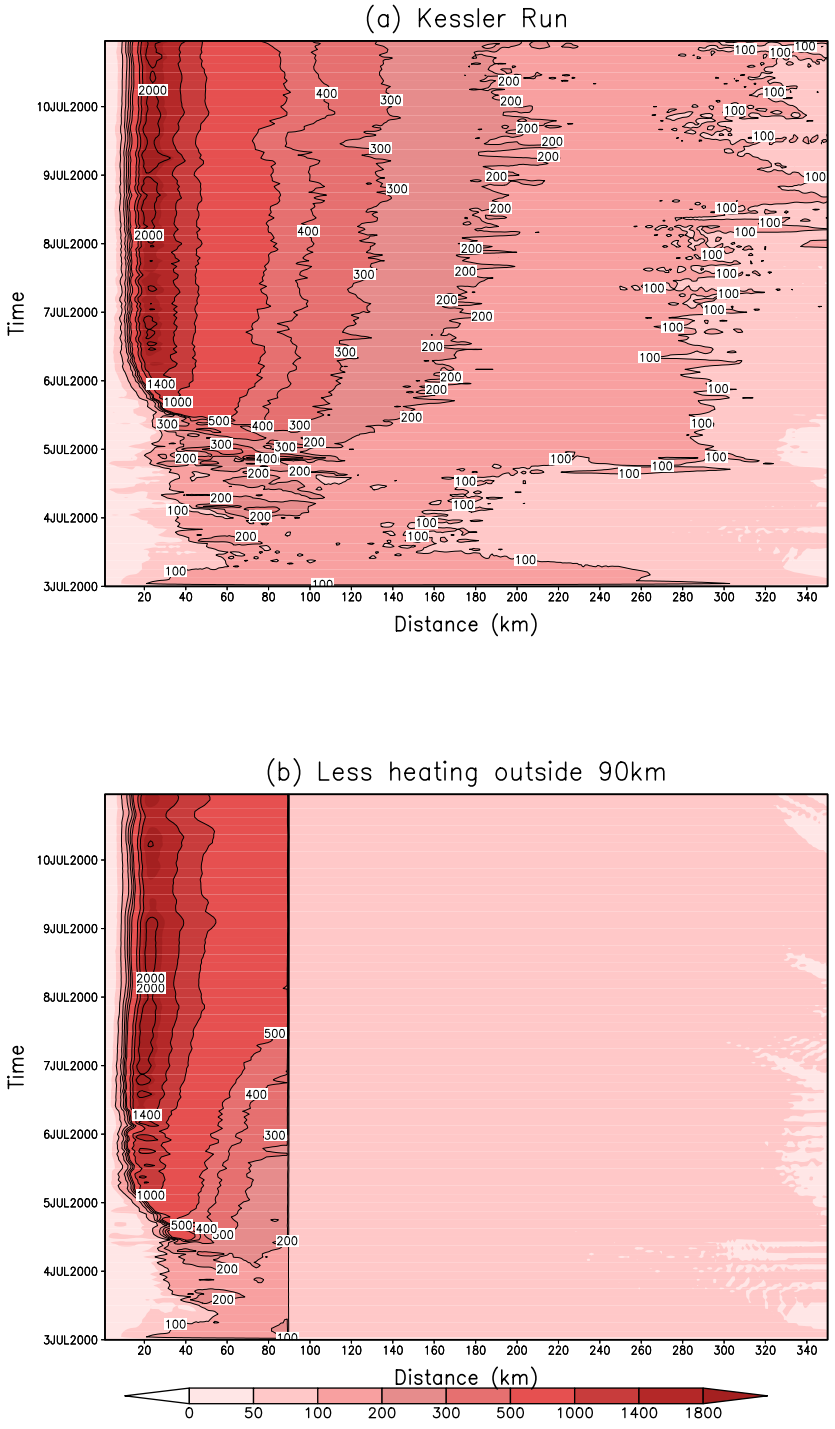

Figure 4.11: Hovmoller diagram of total surface heat flux (color field and contours) for the (a) control run, and (b) the K-heatlt50 run (control run with total surface heat flux less than 50 W/m^2 outside 90 km).

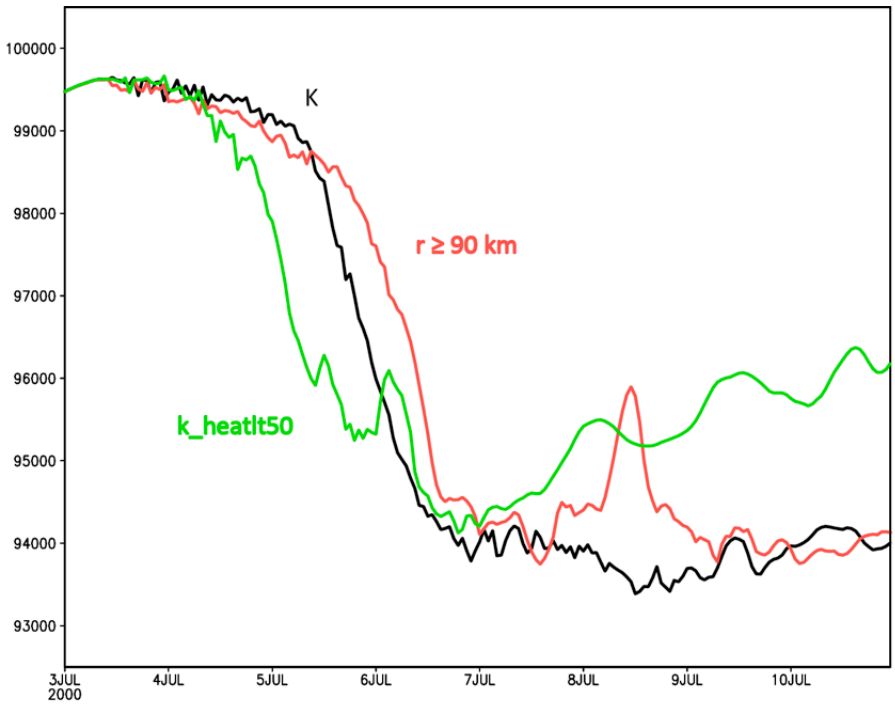

Figure 4.12: Time histories of minimum SLP for control (black), K-heatlt50 (green), and r ≥ 90 km dry tongue (red) simulations.

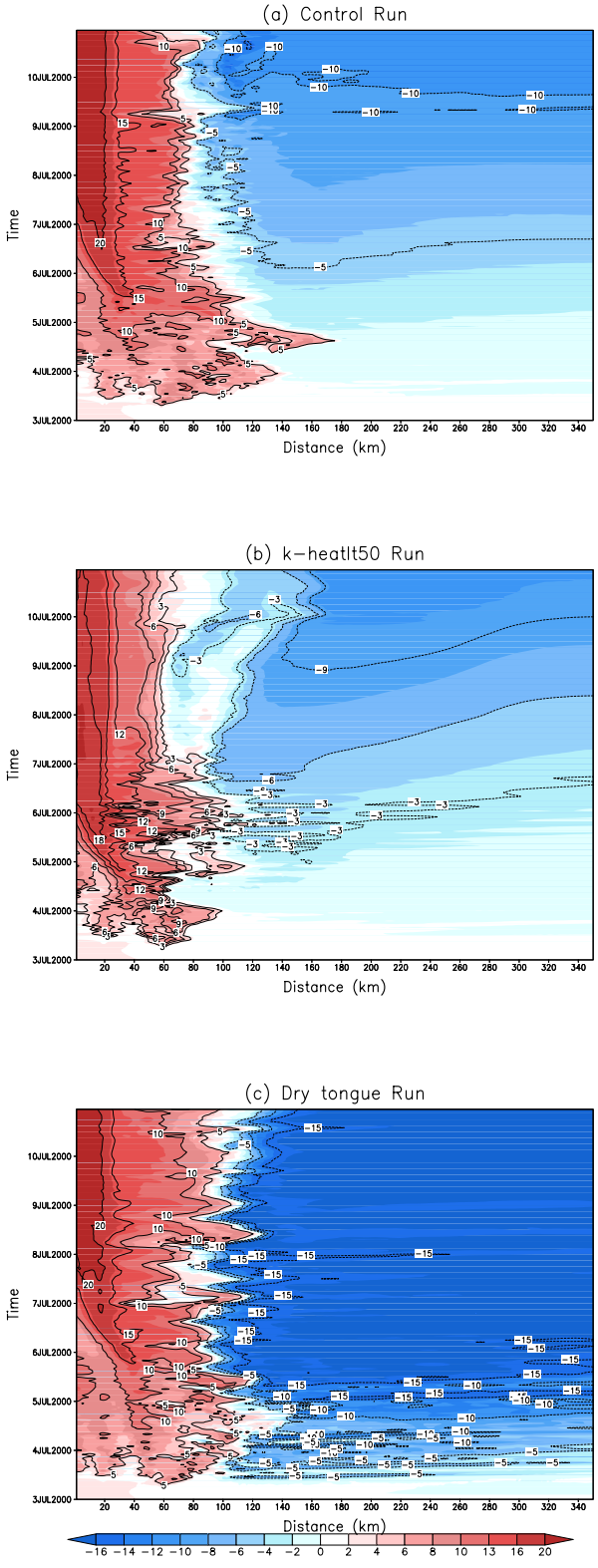

Figure 4.13: Perturbation θ_e (colored and contoured) at 2.75 km height for the (a) control, (b) K-heatlt50, and (c) r ≥ 90 km dry tongue simulations

the context of AAM convergence at low levels.

Take the simulations shown in Figure 4.5 as examples. AAM fields at that time (18 h) for those runs are shown in Figure 4.14. Strong convective activity around 240 ≤ r ≤ 300 km in the K-gt300-outer run is being provoked by the augmented heat flux at larger radii in this experiment, and we see strong upward transport of AAM in that radial range (Figure 4.14b). Yet, this appears to be interfering with the inward transport of momentum. In the control run (Figure 4.14a), the AAM isopleths penetrate much farther inward. Note the 1500 m^2/s isopleth reaches as far inward as r = 100 km within the boundary layer in the control run while it is located around r = 130 km in K-gt300-outer run.

Perhaps the K-gt300-outer storms peripheral convection is encouraging upward instead of horizontal motion, hence interrupting the inward convergence of the AAM. On the inner side of the convective activity, convergence is transporting AAM radially outward, towards the strong updraft. Fifty-four hours later the control run is already in the middle of its RI period (Figure 4.15a). In the lower troposphere, AAM isopleths have shifted inward by a considerable distance. The tight gradient located at about r = 25 km indicates the eyewall updraft is well developed at this time and the absence of a vertical gradient indicates the radial flow is weak. By comparison, the K-gt300-outer run is clearly less organized. At this time, continuing peripheral convection around r = 160 km is blocking the efficient inward transport of AAM.

To summarize, the peripheral convection appears to be able to delay the onset of RI by changing the secondary circulation. Convective activity beyond the inner core disrupts the inflow of high momentum air from its source region radially outward from the core.

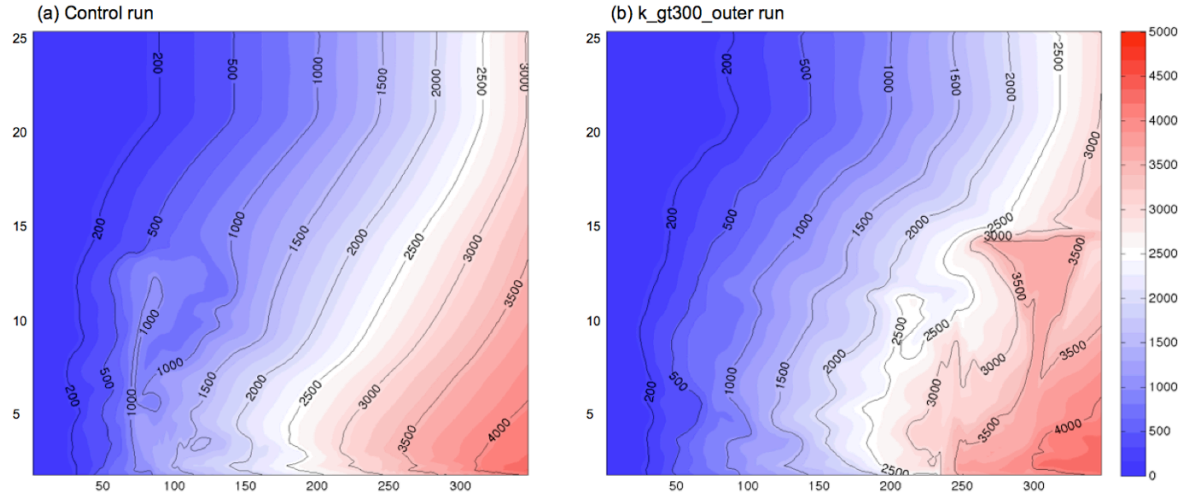

Figure 4.14: Radius vs. height (km) plots of AAM (colored and contoured, in m^2/s) for the (a) control (K), and (b) K-gt300-outer runs

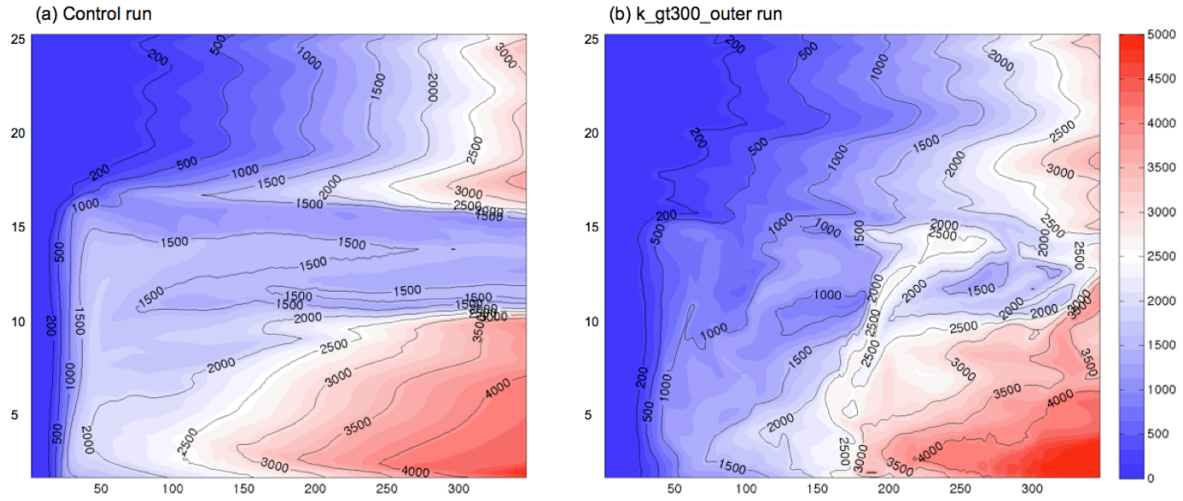

Figure 4.15: As in Figure 4.14 but at 72 h

4.4 Competition between inner and outer convection

We now further explore the competition between convection in the inner and outer core regions through experimentation with the NCR version of the warm rain microphysics. Figure 3.6 demonstrated that, compared to the control microphysics, the NCR scheme can increase the convective activity in these two regions simultaneously. Their effects can be separated by restricting this scheme to different parts of the domain. Two additional simulations are examined here: NCR-gt120km, in which NCR is only applied outside of r = 120 km, and NCR-lt90km, in which NCR is enabled only for r $\leq$ 90 km.

NCR removes all condensation as it forms. As a result, there is no evaporation cooling in the domain. When the NCR scheme acts in the outer region, the convection will not be suppressed as much as in the control run. If the scheme is acting within the inner core, however, the increased heating helps to hasten the construction of the eyewall.

Figure 4.16 shows the time series of minimum SLP in the control run and the three NCR-based simulations. The results are mainly consistent with our expectations. The NCR-gt120km run has a negative effect on spin-up of the storm, as it takes more than 3 days to reach the tipping point. However, the NCR-lt90km case achieves RI at almost the same time as the original NCR storm, despite the suppression of convection at the outer radii.

Their Hovmoller diagrams of perturbation θ_e at the 3 km level provide some clues. During the first 1.5 days, the control and NCR-gt120km (Figures 4.17a, b) storms rather are similar with respect to the strength of convection in the inner core, but they differ with respect to outer convective development. The NCR microphysics makes it easier for convection to form beyond 120 km, however, and we do see activity occurring there that persists for 2.5 days before it starts moving inward. In the control run, the convection also extends to a wide range, but it is weaker than in storm NCR-

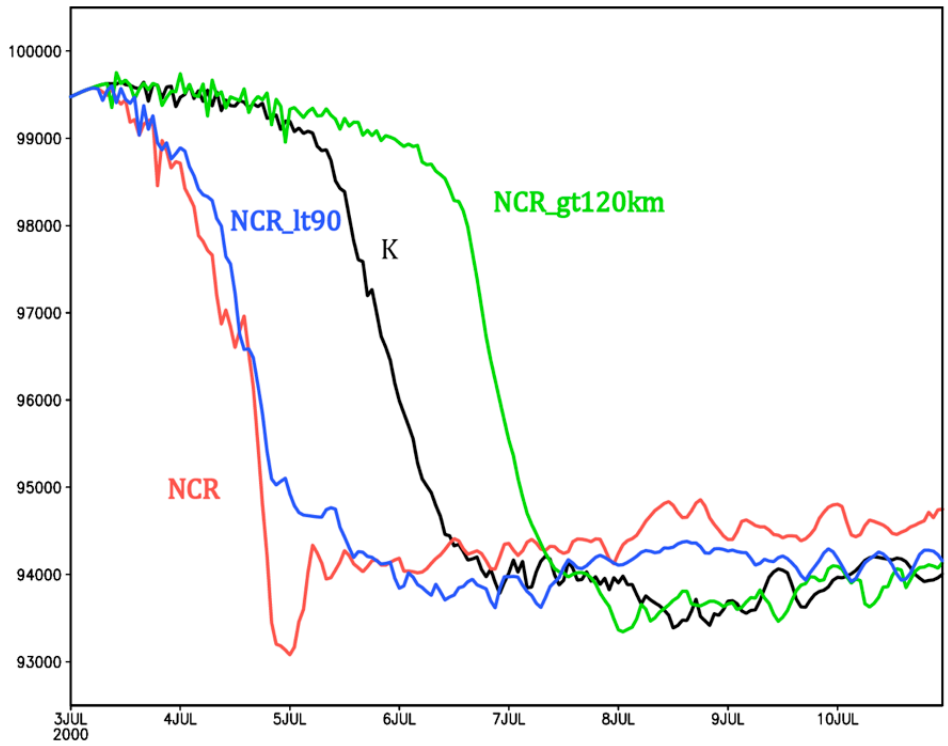

Figure 4.16: Time histories of minimum SLP of for the control K (black), NCR-gt120km (blue), NCR (red) and NCR-lt90km (green) simulations.

gt120km and becomes suppressed earlier. This permits a relatively earlier and more efficient organization of the eyewall.

Outer convection also occurs in the original NCR storm as well (Figure 4.17c), but it moves inward towards the center very quickly, perhaps because the parameterization encourages the rapid development of strong inner core heating which quickly establishes the secondary circulation. Thus, it appears the outer region convection does not delay the onset of RI in this case. The similarity between the RI onsets in the original NCR and NCR-lt90km storms (Figure 4.17d) suggests that suppressing the outer convection does not matter as long as strong inner core convection appears quickly.

To summarize, convective activity in the outer region appears to have a net negative impact on storm organization, and can substantially delay the RI onset time when the inner core convection does not intensify fast enough or remains relatively too weak to compensate. The outer convection has to be suppressed or moved inward to merge with the inner core activity before organization can commence. If the eyewall can become established and stabilized within a short time, however, the influence of the outer convection may be limited. These results apply to axisymmetric storms, which cannot by nature have azimuthal heating asymmetries that also appear to be involved in determining storm intensity.

4.5 Sensitivity to the convection

The preceding experiments have demonstrated that although convection can influence the tipping point, its specific impact depends on its timing, location, strength and so on. In this section, we further explore the sensitivity of storm organization to convection by inserting targeted perturbations into the control run. Specifically, two moist, warm bubbles are introduced at 24 or 36 h, and at various radii. Both are elliptically shaped (Figure 4.18), but one is a small (5 km deep and 10 km wide) and the other is much

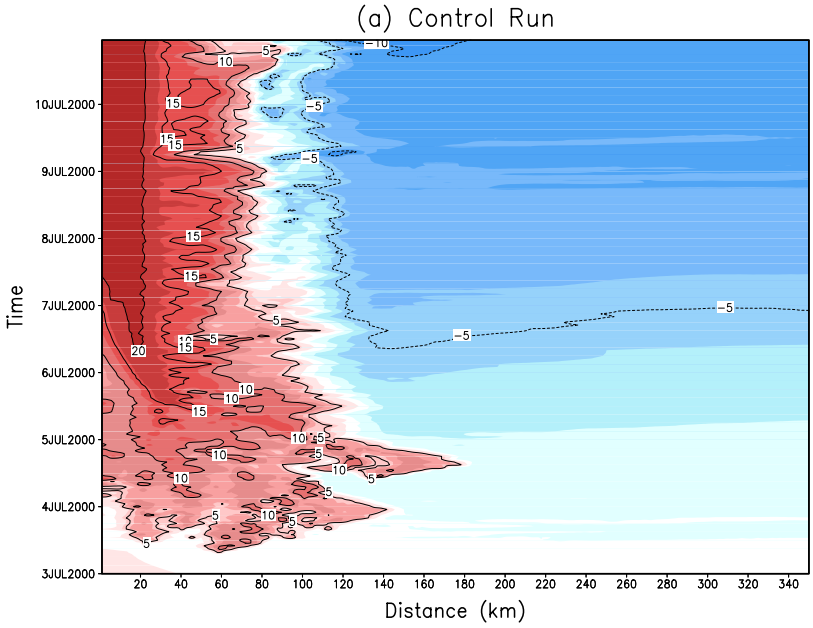
(a) Control Run
Time
10JUL2000
9JUL2000
8JUL2000
7JUL2000
6JUL2000
5JUL2000
4JUL2000
3JUL2000
20 40 60 80 100 120 140 160 180 200 220 240 260 280 300 320 340
Distance (km)

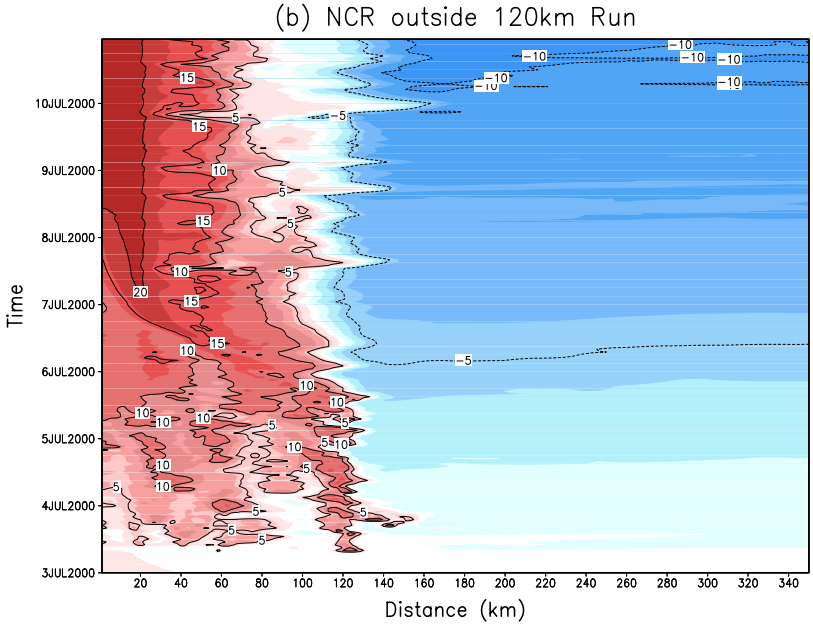
(b) NCR outside 120km Run
Time
10JUL2000
9JUL2000
8JUL2000
7JUL2000
6JUL2000
5JUL2000
4JUL2000
3JUL2000
20 40 60 80 100 120 140 160 180 200 220 240 260 280 300 320 340
Distance (km)

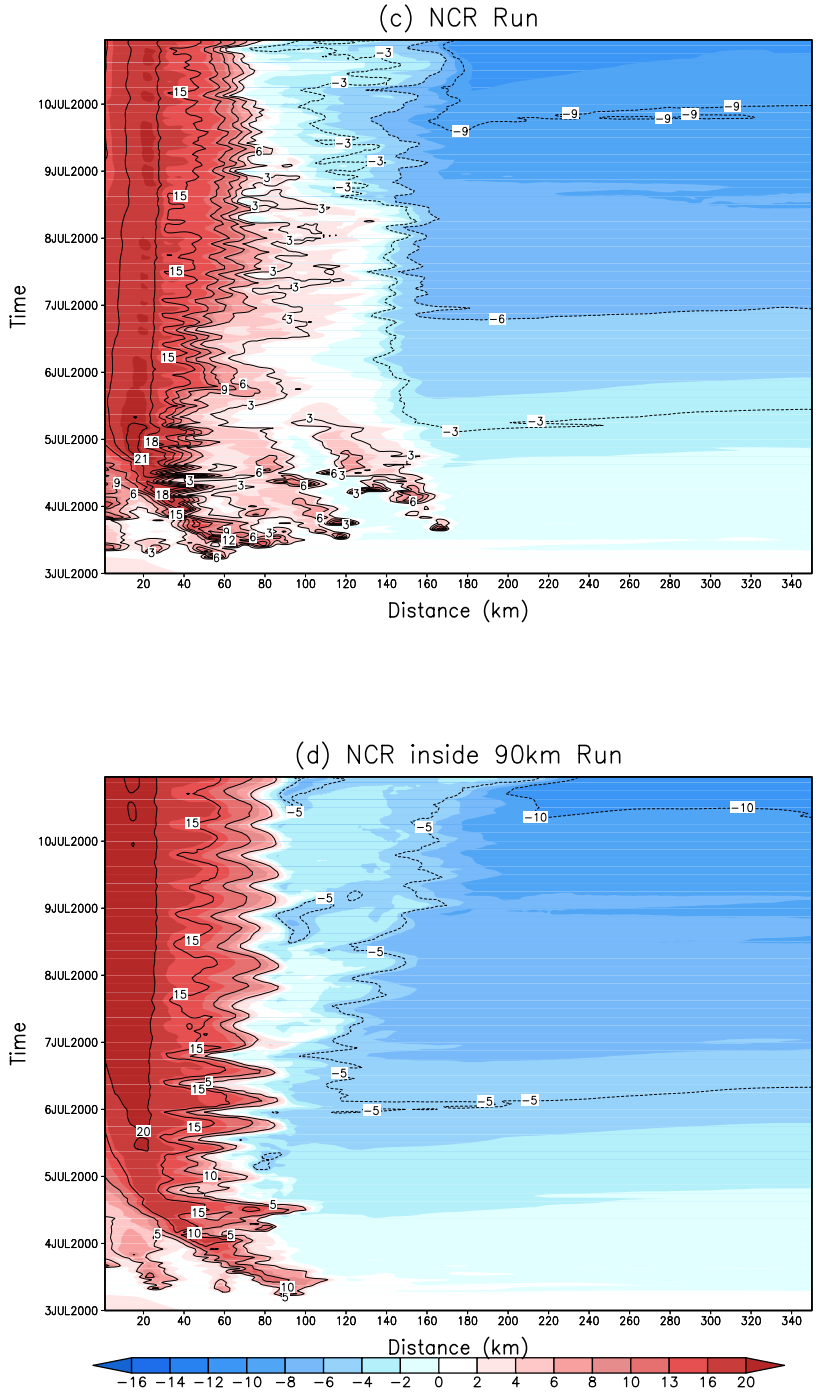

Figure 4.17: Hovmller diagrams of perturbation θ_e at the 3 km level for the (a) control, (b) NCR-gt120km, (c) NCR, and (d) NCR-lt90km runs.

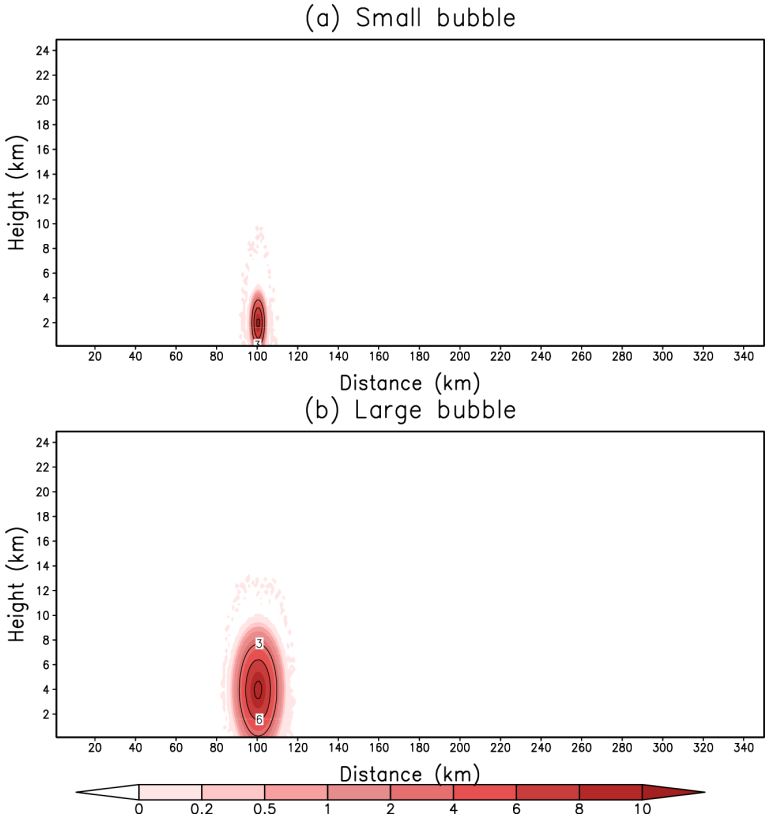

Figure 4.18: Perturbation θ_e (colored and contoured) with respect to the control run for the (a) small bubble, and (b) large bubble, when placed at r = 100 km.

larger (10 km deep and 30 km wide).

As expected, the influence of the bubble on the subsequent TC evolution depends on when and where it was introduced. As an example, we find that at 24 h, the bubble has a greater impact when inserted at r = 150 km compared with r = 100 km. At 36 h, the r = 100 km placement is more effective because the inner core circulation contracts during that time. Henceforth, we will examine perturbations introduced at 36 hours, at a radius of 100 km from the center.

Our initial hypothesis was that the larger bubble would exert a greater influence than the smaller one. The result is exactly the opposite. The small bubble delays RI for about 20 h whereas the large bubble exerts almost no impact on the tipping point

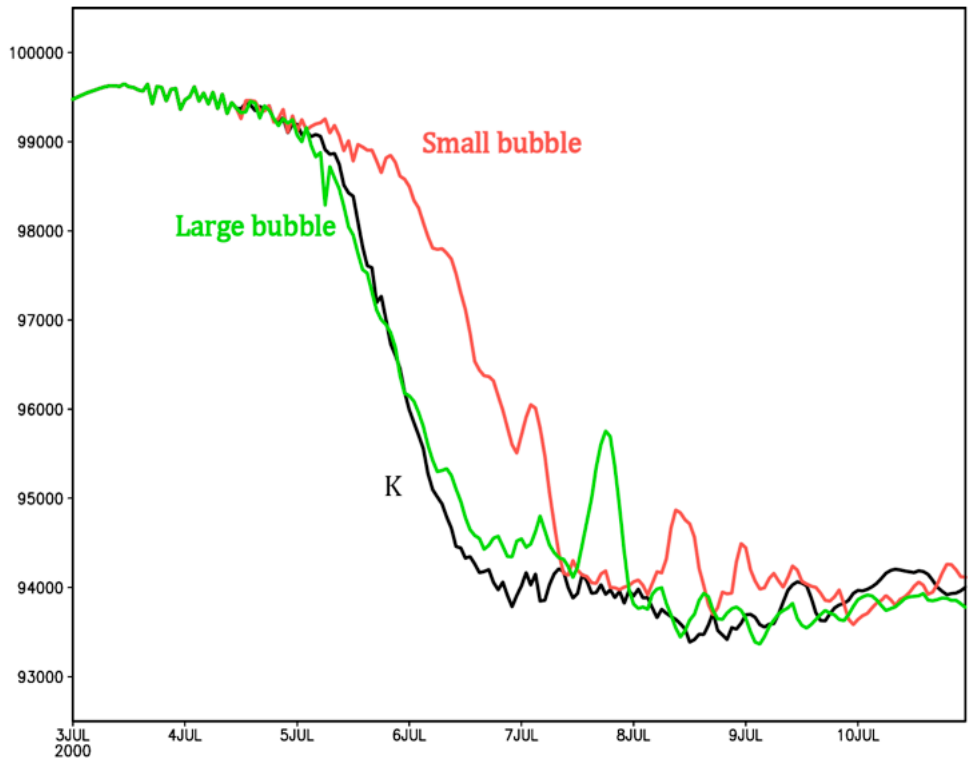

Figure 4.19: Time histories of minimum SLP for the control (black) run, along with runs in which a large (green) and small (red) bubble was added at a radius of 100 km at 36 h.

(Figure 4.19).

The Hovmoller diagrams of perturbation θ_e (Figure 4.20) suggest that neither of the bubble simulations induces substantial convective activity at outer radius, at least not right away. The bubbles themselves disappear 4 or 5 hours after their insertions. Yet, for the small bubble storm (Figure 4.20b), obvious differences do emerge after several hours, as the perturbation sets off a chain of events that makes the eyewall organization slower. This is more apparent in Figure 4.21a, which shows the difference in θ_e between this simulation and the control run. We see differences propagate radially inward and outward immediately after the bubble insertion. It seems that the relatively minor perturbation represented by the small bubble causes enhanced convection a little farther outward (at r = 120 km) by about 12 h after insertion. This

enhanced activity occurs while the inner core convection is weak and, consistent with our previous results, this results in a delay in the final organization of the TC eyewall.

As might be expected, the large bubble (Figures 4.20c, 4.21b) has a more substantial immediate impact than the small perturbation, which spreads quickly inward and outward. The induced convection, however, does not last long, and 12 h later (round 00Z on July 5), θ_e perturbations relative to the control run are actually negative around the insertion radius, indicating a smaller amount of convective activity at that time. None of this has a material impact on the ability of the TC to organize (Figure 4.19). In contrast, note again that the convection following the smaller bubble perturbation in more persistent and influential, despite being somewhat delayed. It is a surprise that such a small perturbation can make such a sizable difference.

As noted by *Smith et al.* (2009), the convergence of AAM is relevant to the spin-up of the vortex. Figure 4.22 shows Hovmoller diagrams of AAM at 1.25 km altitude for the three cases. Keep in mind the simulations are identical prior to 36 h. The convergence of AAM within the boundary layer is almost the same in control run (Figure 4.22a) and the large bubble run (Figure 4.22c) while the small bubble run (Figure 4.22b) clearly contracts slowest. Around 54 h, the AAM of control and large bubble runs suddenly contract. It takes about 8 h for the 1500 m^2/s contour to move from 80 km to 30 km. For the small bubble run, this contour takes 30 h to cover the same distance.

Next, we examine the AAM fields at 38 h, 2 h after the bubble insertion. The small bubble does not make any obvious change to the AAM pattern (Figure 4.23b) relative to the control run (Figure 4.23a). The large bubble run, however, has incited strong convection around r = 100 km (Figure 4.23c). This strong convection continues to strengthen over the next four hours, pushing the AAM inward in the boundary layer (Figure 4.24c).

Yet, something similar is also happening in the control run at this time (Figure

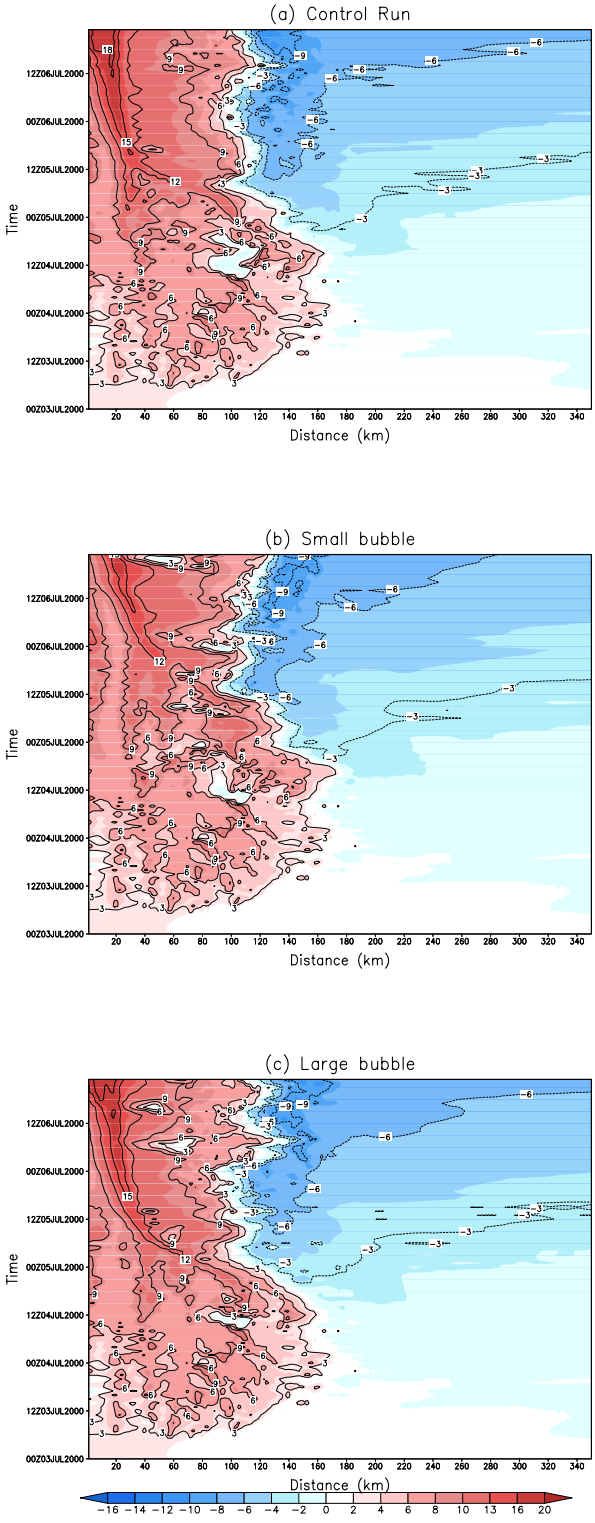

Figure 4.20: Hovmoller diagrams of perturbation θ_e (relative to he initial state) at the 2 km level for the (a) control (K), and simulations in which a (b) small, or (c) large bubble is added at r = 100 km at 36 h.

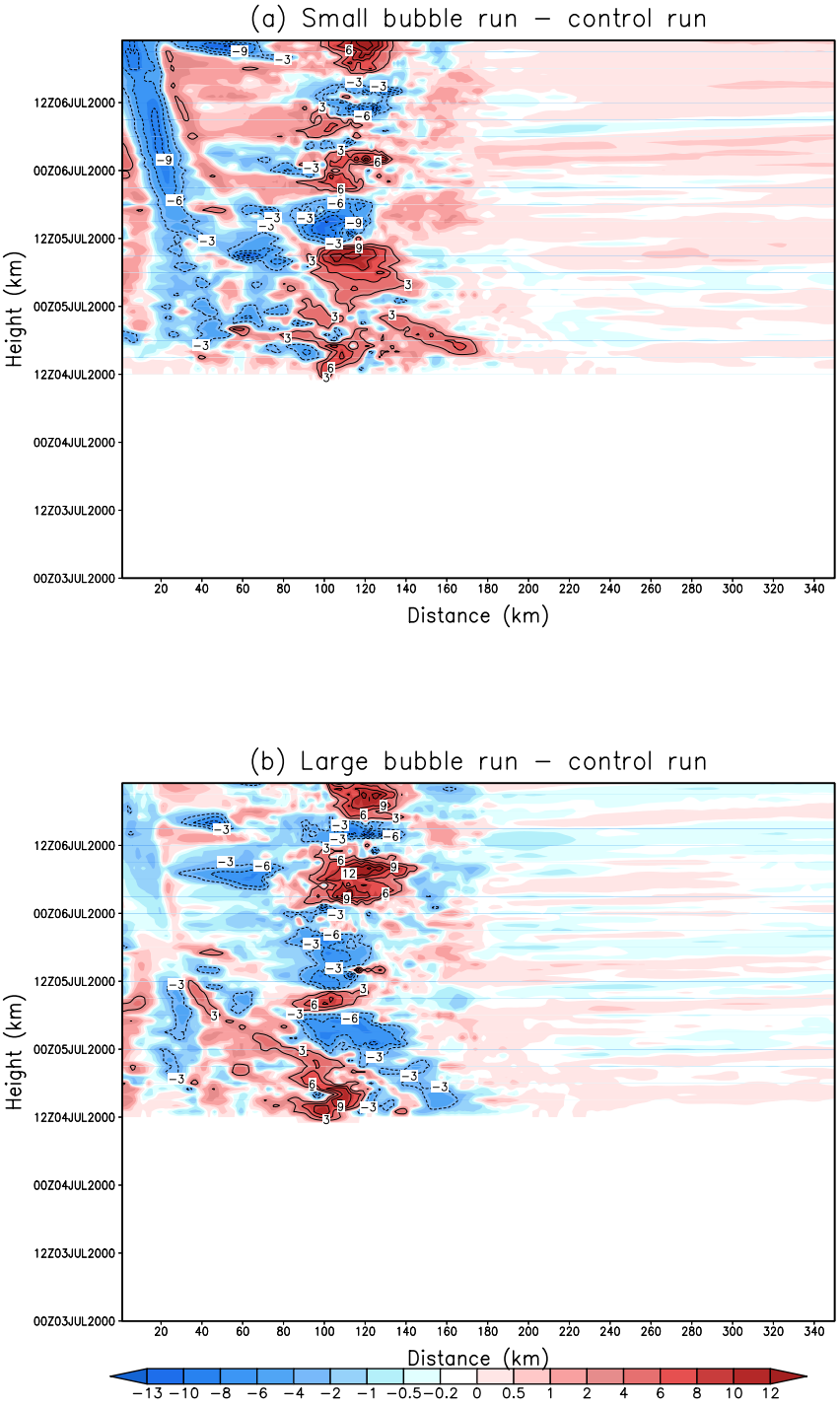

Figure 4.21: Hovmoller diagrams of perturbation θ_e difference with respect to the control run for the (a) small and (b) large bubble runs shown in the previous figure.

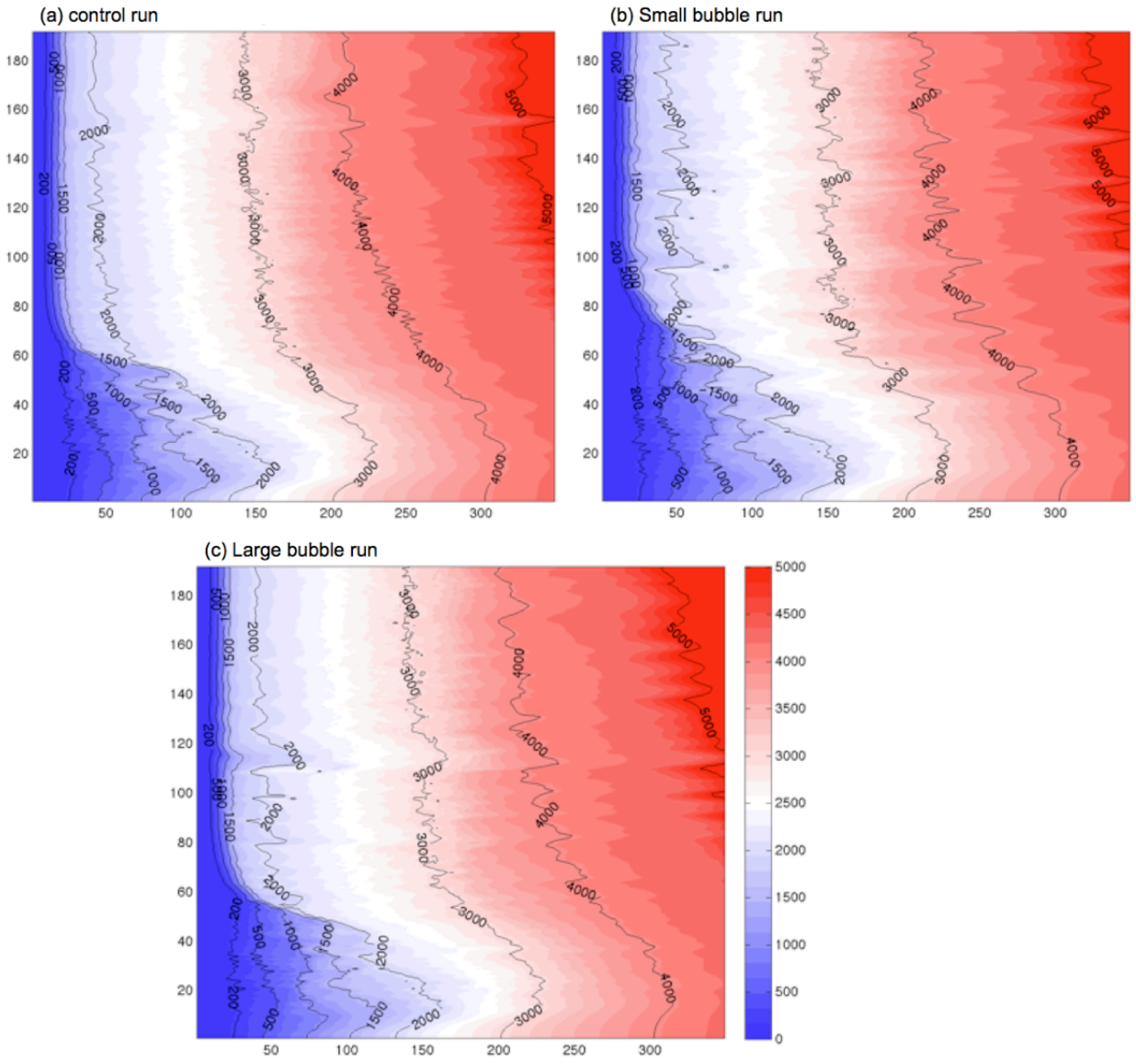

Figure 4.22: Hovmoller diagrams of AAM at 1.25 km height for the (a) control run, and the (a) small and (b) large bubble runs shown in Figure 4.20

4.24a). It turns out that the large bubble does not change the general convergence of AAM relative to that of the control run. The notable distinction between the control and small bubble (Figure 4.24b) runs is the absence of convection in the latter. The small perturbation inserted four hours earlier has modified the storm such that a convective cell that did develop in the control can large bubble cases fails to appear. By this time, it is quite clear that the lower tropospheric AAM isopleths have not progressed inward nearly as far as in the other two storms.

The foregoing suggests that the influence from a single convective development can be very random. Changing the amplitude, size, timing, and even position of the perturbation can alter the results. We just saw that a small bubble, placed at r = 100 km at 36 h, winds up delaying the organization of the inner core vortex. We also performed experiments in which this same small perturbation is inserted at radii of 90, 98, 102 km, and 110 km, instead (not shown). It turned out that the bubble positioned at r = 100 km has the most substantial impact of all. For the 90 km and 110 km placements, the tipping point is almost the same with the control run.

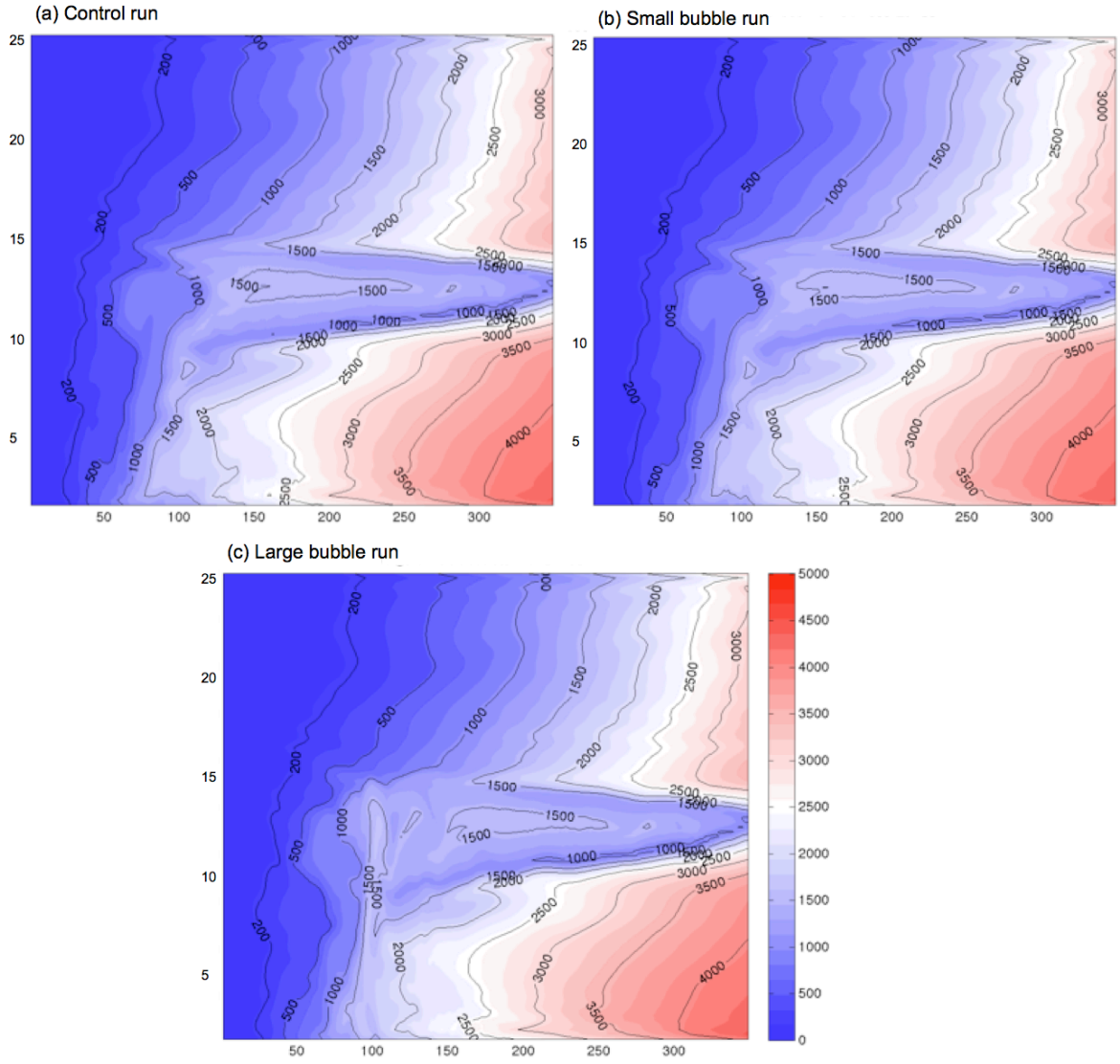

Figure 4.23: AAM at 38 h (a) control run, (b) small bubble run and (c) large bubble run

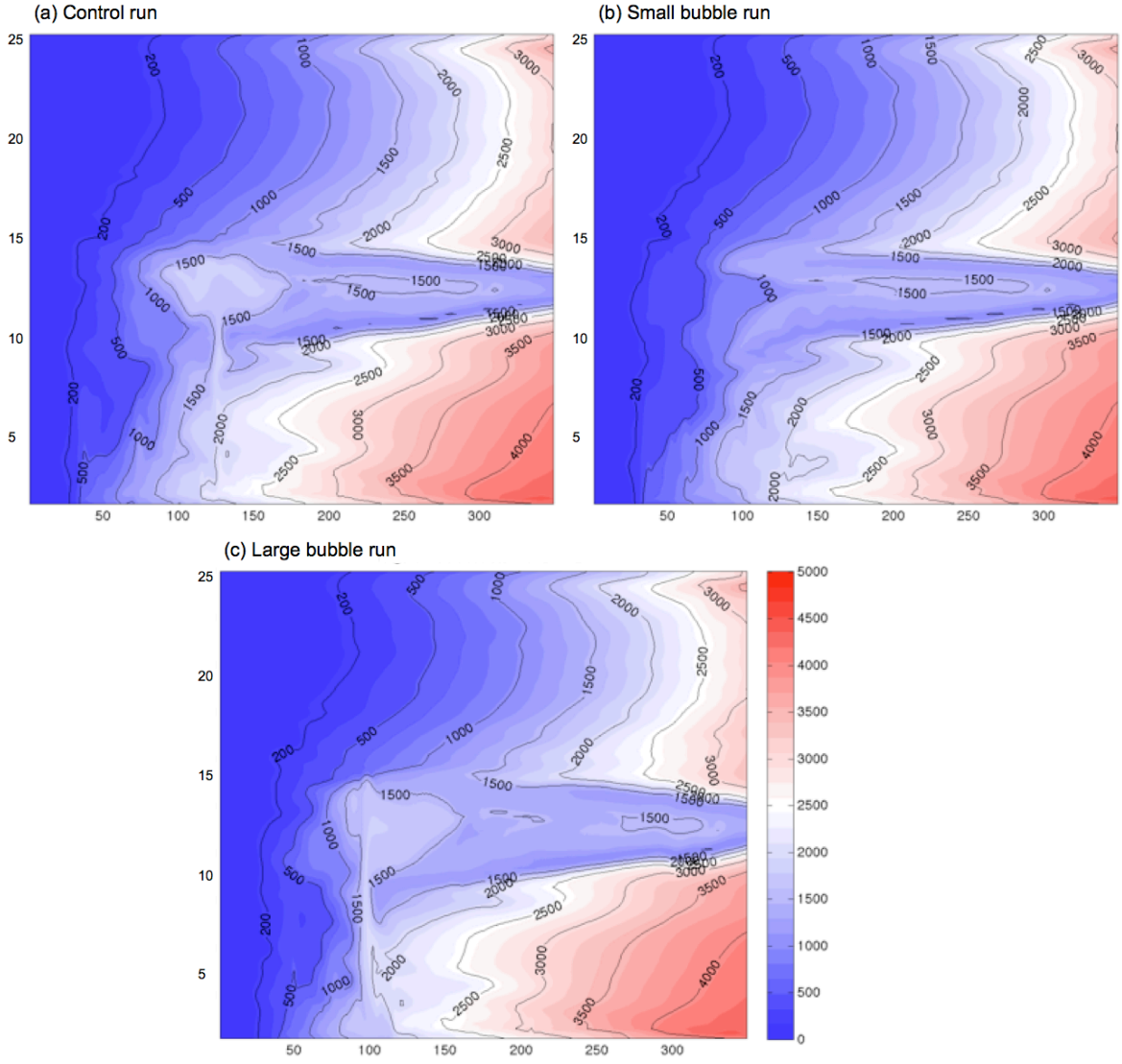

Figure 4.24: AAM at 42 h (a) control run, (b) small bubble run and (c) large bubble run

CHAPTER 5

Conclusion

We have demonstrated that competition between the inner and peripheral convection can determine the tipping point of a model-simulated TC, which we defined as the time at which irreversible organization starts (possibly involving rapid intensification). All the factors mentioned by previous studies, such as tropopause height, initial sounding, microphysics, surface heat fluxes and dry tongues, can influence the tipping point. Most of those factors exert their influence via changing the convective activity.

Emanuel (1986)'s theory predicts that the tropopause height can determine TCs final intensity by controlling the outflow temperature. During the gestation stage, the tropopause height may not be very relevant, as the convection has not yet become very deep. Only when the tropopause is unrealistically low can the TC updrafts reach the tropopause at early stage. In that situation, the outflow will be confined to a lower height, resulting in a warmer outflow. The low tropopause case also results in delayed development. When the tropopause is higher than the equilibrium level for air parcels ascending in the eyewall updraft, however, it appears to exert little or no influence on the storm evolution.

As for cloud microphysics, we saw that adding ice species to the model did not influence the tipping point very much, at least in this model (CM1) and with these initial conditions. As a consequence, we focused on various versions of the warm rain scheme, which is inherently much simpler. Eliminating the evaporation of cloud water and rain drops was shown to substantially change the RI onset time by increasing

the heating rates in the TC. For example, NCR microphysics, in which condensation particles are all removed from the domain immediately upon formation, can shorten the gestation time by about 2 days. The NR run, whose raindrops are removed from the domain, had a tipping point 30 hours earlier than in the control (unmodified warm rain, or Kessler, scheme).

As any given TC organizes, the surface heat flux increases, through the inner core region and especially beneath the eyewall updraft, where the winds are fastest. We demonstrated that bringing about a larger heat flux in the inner core region earlier can also hasten the tipping point. And yet, limiting the heat flux to only 100 W/m^2 for r $\leq$ 80 km in an NCR run was found not to delay RI onset. Thus, it is concluded that the influence of the surface heat flux on the tipping point is indirect.

Our analyses suggest that there are two conditions that need to be satisfied before RI can occur: the vertical structure of the middle troposphere has to become moist adiabatic in the inner core and peripheral convection has to become suppressed or merged with convection in the inner region. Regarding the first condition, we saw that development occurs much more quickly when the initial sounding is moist adiabatic to begin with, other factors being equal. However, this only seems a necessary condition that has to be satisfied before RI can commence. As an example, the Rotunno microphysics and control storms achieved moist adiabatic profiles at midlevels at almost at the same time, and yet the formers tipping point was delayed, possibly owing to the slow suppression of the peripheral convections in that case.

As for the second condition, we saw we could enhance peripheral convection via augmenting the heat flux there and delay final organization of the inner core vortex by about 2 days. One way of suppressing convection beyond the inner core is by making the atmosphere there unfavorable to convection, by adding a midlevel dry tongue. However, the tongue can also harm the organization of the inner core if too much dry air is entrained into the storm vortex. As an example, we saw that when the dry tongue

was initially located at r = 120 km, organization was accelerated relative to the control run, but moving it closer delayed RI.

Outer convective activity influences the organization rate of a TC by impacting the radial influx of absolute angular momentum (AAM). Strong peripheral convection can interrupt the inward flow of AAM by the lower tropospheric winds. For example, in one simulation we artificially increased the total surface heat flux between radii of 200 and 350 km, and the robust convection that resulted transported AAM vertically instead of horizontally. On the inward-facing side of the peripheral overturning, low-level convergence pulled AAM isopleths back outward, postponing the vortex spin-up.

As the tipping point is determined by the convection, and a wide range of gestation periods was found among our simulations, the last thing to do is to test how sensitive the results are to small perturbations. This was done by restarting the control run at different times following insertion of positively buoyant bubbles of various sizes, amplitudes and positions relative to the central axis. We found that the sensitivity can be sizable, and not predictable from the initial dimensions of the disturbance. For example, we saw that a small bubble inserted at a particular place and time caused the storms RI onset to be delayed by 20 hours relative to the control run while a larger perturbation in the same location had little impact. Although it added positive buoyancy to the insertion location, the small bubble appeared to delay peripheral convective activity, actually making it persist longer once it did develop, while the large one did not succeed in changing the circulation in any lasting manner.

This rather surprising result, in combination with the other findings in our study, suggests that the phenomenon of final intensification is sensitively dependent on many factors relating to convection, and thus skillful prediction of RI onset may remain a significant challenge for a long time to come.

Bibliography

Barnes, G. M., E. J. Zipser, D. Jorgensen, and F. M. Jr. (1983), Mesoscale and convective structure of a hurricane rainband, *J. Atmos. Sci.*, *40*, 2125–2137.

Bister, M. (1997), Effect of the coriolis parameter on tropical cyclogenesis: The dominant role of outer convection, in *Preprints, 22d conf. on Hurricanes and Tropical Meteorology*, pp. 553–554, Fort Collins, CO, Amer. Meteor. Soc.

Bister, M. (2001), Effect of peripheral convection on tropical cyclone formation, *J. Atmos. Sci.*, *58*, 34633476.

Braun, S. A., J. A. Sippel, and D. S. Nolan (2012), The impact of dry midlevel air on hurricane intensity in idealized simulations with no mean flow, *J. Atmos. Sci.*, *69*, 236257.

Bryan, G. H., and J. M. Fritsch (2002), Bryan, g. h., and j. m. fritsch, *Mon. Wea. Rev.*, *130*, 2917–2928.

Bryan, G. H., and R. Rotunno (2009), The maximum intensity of tropical cyclones in axisymmetric numerical model simulations, *Mon. Wea. Rev.*, *137*, 17701789.

Charney, J., and A. Eliassen (1964), On the growth of the hurricane depression, *J. Atmos. Sci.*, *21*, 68,075.

Craig, G. C., and S. L. Gray (1996), Cisk or wishe as the mechanism for tropical cyclone intensification, *J. Atmos. Sci.*, *53*, 35283540.

Davis, C. A., and L. F. Bosart (2001), Numerical simulations of the genesis of hurricane diana (1984). part i: Control simulation, *Mon. Wea. Rev.*, *129*, 1859–1881.

Davis, C. A., and L. F. Bosart (2002), Numerical simulations of the genesis of hurricane diana (1984). part ii: Sensitivity of track and intensity prediction, *Mon. Wea. Rev.*, *130*, 1100–1124.

Davis, C. A., and K. A. Emanuel (1991), Potential vorticity diagnostics of cyclogensis, *Mon. Wea. Rev.*, *119*, 1929–1953.

Emanuel, K. A. (1986), An air-sea interaction theory for tropical cyclones. part i: Steady state maintenance, *J. Atmos. Sci.*, *43*, 585–604.

Emanuel, K. A. (1994), *Atmospheric convection*, Oxford University Press: Oxford, UK.

Emanuel, K. A. (1995), Sensitivity of tropical cyclones to surface exchange coefficients and a revised steady-state model incorporating eye dynamics, *J. Atmos. Sci.*, *52*, 39693976.

Emanuel, K. A., N. J. D., and C. S. Bretherton (1994), On large-scale circulations in convecting atmosphere., *Q. J. R. Meteorol. Soc.*, *120*, 1111–1143.

Emanuel, K. A., C. DesAutels, C. Holloway, and R. Korty (2004), Environmental control of tropical cyclone intensity, *J. Atmos. Sci.*, *61*, 843858.

Fovell, R. G. (2004), Adjoint of a parameterized moisture track and intensity forecasts, *Meteor. Atmos. Phys.*, *86*, 173–194.

Fovell, R. G., K. L. Corbosiero, and H. C. Kuo (2009), Cloud microphysics impact on hurricane track as revealed in idealized experiments, *J. Atmos. Sci.*, *66*, 1764–1778.

Fovell, R. G., K. L. Corbosiero, A. Seifert, and K.-N. Liou (2010), Impact of cloud-radiative feedback on hurricane track, *Geophysical Research Letters*, *37*, L07,808.

Hausman, S. A., K. V. Ooyama, and W. H. Schubert (2006), Potential vorticity structure of simulated hurricanes, *J. Atmos. Sci.*, *63*, 87–107.

Hill, K. A., and G. M. Lackmann (2009), Influence of environmental humidity on tropical cyclone size, *Mon. Wea. Rev.*, *137*, 32943315.

Holland, G. J. (1983), Angular momentum transports in tropical cyclones, *Q. J. R. Meteorol. Soc.*, *109*, 187209.

Holliday, C. R., and A. H. Thompson (1979), Climatological characteristics of rapidly intensifying typhoons, *Mon. Wea. Rev.*, *107*, 10221034.

Holton, J. R. (2004), *An introduction to dynamic meteorology*, Academic Press: London.

Hoskins, B. J., M. E. McIntyre, and A. W. Robertson (1985), On the use and significance of isentropic potential vorticity maps, *Quart. J. Roy. Meteor. Soc.*, *111*, 887–946.

Kessler, E. (1969), On the distribution and continuity of water substance in atmospheric circulations, *Amer. Meteor. Soc.*, *32*, 84.

Li, X., and Z. Pu. (2008), Sensitivity of numerical simulation of early rapid intensification of hurricane emily (2005) to cloud microphysical and planetary boundary layer parameterizations, *Mon. Wea. Rev.*, *136*, 48194838.

Lord, S. J., H. E. Willoughby, and J. M. Piotrowicz (1984), Role of a parameterized ice?phase microphysics in an axisymmetric, nonhydrostatic tropical cyclone model, *J. Atmos. Sci.*, *41*, 28362848.

May, P. T., and G. J. Holland (1999), The role of potential vorticity generation in tropical cyclone rainbands, *J. Atmos. Sci.*, *56*, 1224–1228.

Molinari, J., S. Skubis, F. A. D. Vollaro, and H. E. Willoughby (1998), Potential vorticity analysis of tropical cyclone intensification, *J. Atmos. Sci.*, *55*, 2632–2644.

Nolan, D. S., and L. D. Grasso (2003), Nonhydrostatic, three-dimensional perturbations to balanced, hurricane-like vorticies. part ii: Symmetric response and nonlinear simulations, *J. Atmos. Sci.*, *60*, 27172745.

Nolan, D. S., C. D. Zhang, and S. H. Chen (2007), Dynamics of the shallow circulation around itcz regions, *J. Atmos. Sci.*, *64*, 2262–2285.

Ooyama, K. (1964), A dynamical model for the study of tropical cyclone development, *Geophys. Int.*, *4*, 187–198.

Powell, M. D. (1990a), Boundary layer structure and dynamics in outer hurricane rainbands. part i: Mesoscale rainfall and kinematic structure, *Mon. Wea. Rev.*, *188*, 891–917.

Powell, M. D. (1990b), Boundary layer structure and dynamics in outer hurricane rainbands. part ii: Downdraft modification and mixed layer recovery, *Mon. Wea. Rev.*, *118*, 918–938.

Rotunno, R., and K. A. Emanuel (1987), An air-sea interaction theory for tropical cyclones. part ii: Evolutionary study using a nonhydrostatic axisymmetric numerical model, *J. Atmos. Sci.*, *44*, 542–561.

Smith, R. K., M. T. Montgomery, and N. V. Sang (2009), Tropical cyclone spin-up revisited, *Q. J. R. Meteorol. Soc.*, *642*, 1321–1335.

Stern, D. P., and D. S. Nolan (2012), On the height of the warm core in tropical cyclones, *J. Atmos. Sci.*, *69*, 16571680.

Tao, W. K., and J. Simpson (1993), The goddard cumulus ensemble model. part i: Model description, *Terr. Atmos. Oceanic Sci.*, *4*, 35–72.

Thompson, G., R. M. Rasmussen, and K. Manning (2004), Explicit forecasts of winter

precipitation using an improved bulk microphysics scheme. part i: Description and sensitivity analysis, *Mon. Wea. Rev.*, *132*, 519–542.

Wang, Y. (2002), An explicit simulation of tropical cyclones with a triply nested movable mesh primitive equations model-tcm3. part ii: Model refinements and sensitivity to cloud microphysics parameterization, *Mon. Wea. Rev.*, *130*, 30223036.

Wang, Y. (2009), How do outer spiral rainbands affect tropical cyclone structure and intensity?, *J. Atmos. Sci.*, *66*, 12501273.

Weatherford, C. L., and W. M. Gray (1988), Typhoon structure as revealed by aircraft reconnaissance. part i: Data analysis and climatology, *Mon. Wea. Rev.*, *116*, 1032.

Zhu, T., and D. L. Zhang (2006), Numerical simulation of hurricane bonnie (1998). part ii: Sensitivity to varying cloud microphysical processes, *J. Atmos. Sci.*, *63*, 109–126.